

A framework for estimating global-scale river discharge by assimilating satellite altimetry

Menaka Revel¹, Daiki Ikeshima², Dai Yamazaki¹, and Shinjiro Kanae²

¹University of Tokyo

²Tokyo Institute of Technology

January 20, 2023

Abstract

Understanding spatial and temporal variations in terrestrial waters is key to assessing the global hydrological cycle. The future Surface Water and Ocean Topography (SWOT) satellite mission will observe the elevation and slope of surface waters at <100 m resolution. Methods for incorporating SWOT measurements into river hydrodynamic models have been developed to generate spatially and temporally continuous discharge estimates. However, most of SWOT data assimilation studies have been performed on a local scale. We developed a novel framework for estimating river discharge on a global scale by incorporating SWOT observations into the CaMa-Flood hydrodynamic model. The local ensemble transform Kalman filter with adaptive local patches was used to assimilate SWOT observations. We tested the framework using multi-model runoff forcing and/or inaccurate model parameters represented by corrupted Manning's coefficient. Assimilation of virtual SWOT observations considerably improved river discharge estimates for continental-scale rivers at high latitudes (>50°) and also downstream river reaches at low latitudes. High assimilation efficiency in downstream river reaches was due to both local state correction and the propagation of corrected hydrodynamic states from upstream river reaches. Accurate global river discharge estimates were obtained (Kling–Gupta efficiency [KGE] > 0.90) in river reaches with > 270 accumulated overpasses per SWOT cycle when no model error was assumed. Introducing model errors decreased this accuracy (KGE [?] 0.85). Therefore, improved hydrodynamic models are essential for maximizing SWOT information. These synthetic experiments showed where discharge estimates can be improved using SWOT observations. Further advances are needed for data assimilation on global-scale.

1 **A framework for estimating global-scale river discharge**
2 **by assimilating satellite altimetry**

3
4 **Menaka Revel^{1*}, Daiki Ikeshima^{2*}, Dai Yamazaki¹, and Shinjiro Kanae²**

5 ¹ Institute of Industrial Science, The University of Tokyo, 4-6-1, Komaba, Meguro-ku, Tokyo
6 153-8505, Japan

7 ² Department of Civil and Environmental Engineering, Tokyo Institute of Technology, 2-12-1-
8 M1-6 O-okayama, Meguro-ku, Tokyo 152-8552, Japan

9
10 * these authors equally contributed to the manuscript.

11 Corresponding author: Menaka Revel (menaka@rainbow.iis.u-tokyo.ac.jp)

12
13 **Key Points:**

- 14 • A framework for assimilating satellite altimetry into a global river hydrodynamic model
15 was developed to estimate river discharge globally.
- 16 • Virtual experiments for future SWOT satellite suggest discharge in downstream reaches
17 of continental rivers can be accurately estimated.
- 18 • Correct hydrodynamic parameterization will enhance the accuracy of river discharge
19 estimates for the upstream reaches of rivers at low latitudes when SWOT observations
20 become available.

22 **Abstract**

23 Understanding spatial and temporal variations in terrestrial waters is key to assessing the global
24 hydrological cycle. The future Surface Water and Ocean Topography (SWOT) satellite mission
25 will observe the elevation and slope of surface waters at <100 m resolution. Methods for
26 incorporating SWOT measurements into river hydrodynamic models have been developed to
27 generate spatially and temporally continuous discharge estimates. However, most of SWOT data
28 assimilation studies have been performed on a local scale. We developed a novel framework for
29 estimating river discharge on a global scale by incorporating SWOT observations into the CaMa-
30 Flood hydrodynamic model. The local ensemble transform Kalman filter with adaptive local
31 patches was used to assimilate SWOT observations. We tested the framework using multi-model
32 runoff forcing and/or inaccurate model parameters represented by corrupted Manning's
33 coefficient. Assimilation of virtual SWOT observations considerably improved river discharge
34 estimates for continental-scale rivers at high latitudes ($>50^\circ$) and also downstream river reaches at
35 low latitudes. High assimilation efficiency in downstream river reaches was due to both local state
36 correction and the propagation of corrected hydrodynamic states from upstream river reaches.
37 Accurate global river discharge estimates were obtained (Kling–Gupta efficiency [KGE] > 0.90)
38 in river reaches with > 270 accumulated overpasses per SWOT cycle when no model error was
39 assumed. Introducing model errors decreased this accuracy (KGE ≈ 0.85). Therefore, improved
40 hydrodynamic models are essential for maximizing SWOT information. These synthetic
41 experiments showed where discharge estimates can be improved using SWOT observations.
42 Further advances are needed for data assimilation on global-scale.

43 **Plain Language Summary**

44 River discharge is an important indicator for managing the world’s freshwater resources. Advances
45 in computing technology have facilitated the development of hydrodynamic models, which can be
46 used to predict river water states and compensate for the lack of in-situ observation facilities.
47 However, these models have inherent limitations, including the simplified physics, forcing errors,
48 and inaccurate parameters. Satellite observations, such as those from the Surface Water and Ocean
49 Topography (SWOT) mission, may be incorporated to improve these models. Because the SWOT
50 satellite is due for launch in 2021, assessing the potential benefits of incorporating SWOT
51 observations into global hydrodynamic models is essential. Therefore, we performed observation
52 assimilation experiments using a technique known as Kalman filtering, which assesses model
53 uncertainty and expected observation errors. Note that SWOT observations are not recorded
54 continuously; therefore, the hydrodynamic model was used to extrapolate water states in time and
55 space. We found that incorporating SWOT observations provided accurate river discharge
56 estimates, in continental-scale rivers. Furthermore, correcting model parameters will considerably
57 improve river discharge estimates. This framework may be used to generate accurate global river
58 discharge estimates when SWOT observations become available. Therefore, these methods can be
59 helpful for mitigating conflicts in transboundary river basins (e.g., Mekong).

60 1. Introduction

61 River discharge is a key variable for understanding the global hydrological cycle and
62 assessing water resources (Oki & Kanae, 2006). Networks of *in situ* stream gauging stations are a
63 fundamental data source for estimating spatial and temporal variations in the discharge of major
64 rivers worldwide. However, the numbers of accessible stream gauges are not adequate to fully
65 understand details of the global hydrological cycle, and real-time access to gauged discharge data
66 is usually available only in developed countries. Although remote sensing of river discharge is a
67 challenging research topic, recent advances in satellite observation technology are expected to
68 enhance our understanding of river discharge variation on the global scale (Marcus & Fonstad,
69 2010).

70 The Surface Water and Ocean Topography (SWOT) satellite is a next-generation satellite
71 altimetry mission due to launch in 2021 (Durand et al., 2010). This satellite will measure two-
72 dimensional water surface elevation (WSE) across its 120 km wide swath using a Ka-band radar
73 interferometer. The WSE of rivers and lakes will be measured at < 100 m spatial resolution over
74 5–10 day intervals, depending on the satellite’s location during its 21-day repeat-cycle orbit
75 (Biancamaria et al., 2016). The fine spatial resolution will ensure that rivers wider than 50–100 m
76 (Pavelsky et al., 2014) and lakes larger than 1–5 ha (Lee et al., 2010) are included, providing
77 information on surface-water dynamics in unprecedented detail. In addition to WSE data, the high-
78 resolution measurements will also provide accurate information on water -surface slopes across
79 river networks.

80 Although the SWOT satellite will not measure river discharge directly, algorithms to
81 estimate discharge from variables that will be measured by SWOT (e.g., WSE, slope, and width)
82 have been developed (Durand et al., 2016; Garambois & Monnier, 2015; Gleason & Smith, 2014).
83 These algorithms can estimate river discharge in some ungauged rivers with approximately 35%
84 root mean square error (Bonnema et al., 2016; Durand et al., 2016). However, due to the limited
85 frequency of observations, these satellite-based methods cannot produce spatially and temporally
86 continuous estimates of river discharge. Consequently, recent research has investigated whether
87 SWOT measurements can be integrated into river hydrodynamic models (Andreadis et al., 2007;
88 Biancamaria et al., 2011; Brêda et al., 2019; Pedinotti et al., 2014).

89 The potential benefits of assimilating future SWOT observations into river hydrodynamic
90 models have been assessed using observing system simulation experiments (OSSEs) (Andreadis
91 et al., 2007). Because the SWOT satellite has not yet been launched, synthetic SWOT observations
92 were generated using a river hydrodynamics model that was assumed to be ‘true.’ Then, the
93 synthetic observations were assimilated into a corrupted hydrodynamics model. The data
94 assimilation framework was evaluated by comparing the estimated river discharge improved by
95 the assimilation against the ‘true’ simulation. Some SWOT data assimilation methods have already
96 been developed and tested in several river basins, including a 50 km reach of the Ohio River
97 (Andreadis et al., 2007), the main-stem of the Ob River (Biancamaria et al., 2011), the Niger River
98 (Munier et al., 2015; Pedinotti et al., 2014), the entire Congo basin (Revel et al., 2019), and the
99 Amazon basin (Brêda et al., 2019; Emery et al., 2019). These studies demonstrated that SWOT
100 observations had the potential to improve river hydrodynamic simulations and estimate river
101 discharge and/or hydrodynamic parameters continuously in space and time. However, previous
102 SWOT assimilation studies used regional-scale river models or expensive data assimilation
103 algorithms, which cannot be applied easily on a global scale. In addition, a global-scale

104 hydrodynamic model that can assess WSE measurements rapidly is needed because SWOT WSE
 105 measurements will be generated daily. To evaluate the effectiveness of data assimilation in global-
 106 scale using SWOT observation, a global-scale study with computationally efficient river model
 107 and data assimilation algorithm are essential.

108 This study evaluated the use of SWOT observations to estimate river discharge on a global
 109 scale. We developed a new data assimilation framework for integrating SWOT observations into
 110 a global river hydrodynamic model. Using the Catchment-based Macro-scale Floodplain (CaMa-
 111 Flood) global hydrodynamic model (Yamazaki et al., 2011) and a highly efficient data assimilation
 112 method called the local ensemble transform Kalman filter (LETKF; Hunt et al., 2007), we
 113 assimilated global-scale data at a reasonable computational cost. A detailed description of the data
 114 assimilation framework is provided in Section 2. The experimental conditions and evaluation
 115 methods are presented in Section 3. Results are explained and discussed in Section 4, and Section
 116 5 includes a summary and discussion.

117 **2. Development of Data Assimilation Framework**

118 **2.1 SWOT data assimilation framework**

119 We developed a new global-scale data assimilation framework for hydrodynamic modeling
 120 to estimate river discharge using SWOT altimetry data. The CaMa-Flood hydrodynamic model
 121 formed the core of our global data assimilation framework. This framework was designed to
 122 assimilate WSE data gathered by the SWOT satellite. We used the LETKF, an ensemble Kalman
 123 filter (EnKF) variant, as our data assimilation algorithm. In addition, we used a physically-based
 124 adaptive localization method to utilize as many observations as possible.

125 Figure 1 shows the workflow for our data assimilation framework. First, from the initial
 126 water state in time step T (x_T^a in Figure 1), the water state ($x_{T+\Delta T}^f$ in Figure 1) for time $T + \Delta T$
 127 was simulated using the CaMa-Flood model for the duration ΔT , forced by the land surface runoff
 128 data at the corresponding time. Here, multiple forecasted water states were prepared from the
 129 different initial water conditions and runoffs. An ensemble of forecasted water states is essential
 130 for assessing prior error covariance in LETKF assimilation procedure. The corrected water state
 131 at $T + \Delta T$ ($x_{T+\Delta T}^a$ in Figure 1) was derived by combining SWOT observations and the ensemble
 132 of forecasted water states using the LETKF algorithm, taking the model variance and observation
 133 error into account. The corrected water state was used as the initial water state for the next
 134 simulation. At the beginning of the simulation ($T = 0$), ensembles were based on the spin-up
 135 simulation from the previous year.

136 **2.2 River hydrodynamics model: CaMa-Flood**

137 We used the CaMa-Flood hydrodynamic model (Yamazaki et al., 2011, 2012, 2013) to
 138 form the core of our data assimilation framework. The CaMa-Flood model receives runoff from a
 139 land surface model (LSM) as input forcing (i.e., the quantity of water entering a river from a unit
 140 land area in mm/day) and simulates river and floodplain hydrodynamics (i.e., river discharge,
 141 WSE, inundated area, and surface water storage) on a global scale. The spatial resolution of the
 142 CaMa-Flood model, which was set to 0.25° in this study, is coarser than that of two-dimensional
 143 flood inundation models (typically <1 km; Bates et al., 2010). Instead of solving two-dimensional
 144 floodplain flows at high resolution, the CaMa-Flood model simulates floodplain inundation

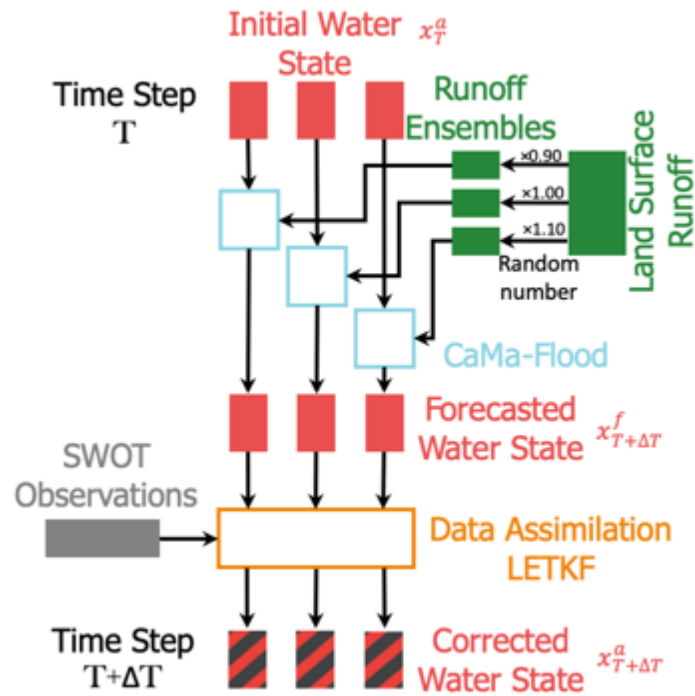


Figure 1: Workflow for the Surface Water and Ocean Topography (SWOT) data assimilation framework.

145 dynamics using sub-grid topography parameters delineated from fine-resolution topography.
 146 Whereas the water mass balance (i.e., surface water storage and river discharge) is calculated at
 147 coarse-grid resolution, the complex floodplain inundation is represented by diagnostic sub-grid
 148 physics. Therefore, the CaMa-Flood model achieves computationally efficient simulations of
 149 global-scale river hydrodynamics. The CaMa-Flood model calculates river discharge using a local
 150 inertial flow equation (computationally efficient modification of the shallow water equation)
 151 (Bates et al., 2010; Yamazaki et al., 2013). Because the pressure term is included in the local
 152 inertial equation, river discharge is estimated based on the water surface slope. This is a key
 153 difference between the CaMa-Flood model and conventional global river models, which use a
 154 kinematic-wave flow equation that neglects the pressure term. Combining the sub-grid flood
 155 inundation scheme and the local inertial flow equation generates a realistic representation of the
 156 WSE in river channels and floodplains. A previous study confirmed that WSE measurements
 157 obtained from simulations that used the CaMa-Flood model were similar to those observed using
 158 satellite altimetry (Yamazaki et al., 2012). Therefore, we chose the CaMa-Flood model to form
 159 the hydrodynamics core of our data assimilation framework. In this study, we used the latest
 160 version of the CaMa-Flood model (ver. 3.96), which integrates highly accurate state-of-the-art
 161 global topography datasets, MERIT DEM and MERIT Hydro (Yamazaki et al., 2017, 2019).

162 2.3 Input runoff forcing

163 In this study, we generated ensembles of forecasted water states using CaMa-Flood to
 164 calculate the error covariance, in accordance with the LETKF data assimilation algorithm. We
 165 generated the ensemble of forecasts using different runoffs (Figure 1) as input forcing for the
 166 CaMa-Flood model. The number of ensemble members was set to 18, in accordance with the
 167 computational cost and recommended minimum number of ensembles for the LETKF algorithm

168 CaMa-Flood hydrodynamic model has a higher computational cost than the data assimilation
169 algorithm, although the number of Monte Carlo sampling errors decreases as the number of
170 ensembles increases (Evensen, 2009). In addition, more than 10 ensembles should be used with
171 the LETKF algorithm (Miyoshi et al., 2007). Therefore, we prepared 18 different runoffs from a
172 multi-model runoff project named Earth2Observe “Global Earth Observation for Integrated Water
173 Resource Assessment” (E2O), the tier-2 water resources reanalysis (WRR2) development project
174 (Dutra et al., 2017). The multi-model runoff data were simulated using bilinear interpolated ERA-
175 interim meteorological data with topographic temperature correction and Multi-Source Weighted-
176 Ensemble Precipitation data. There were eight runoff outputs from different LSMs or Global
177 Hydrological Models (GHMs). We used runoff outputs from Hydrology Tiled ECMWF Scheme
178 for Surface Exchanges over Land (HTESSEL) LSM as “virtual truth” in our experiments because
179 combining the HTESSEL and CaMa-Flood models produces reliable results (Dutra et al., 2017).
180 We treated remaining runoff outputs from E2O WRR2 as “corrupted” runoff inputs. PCR-
181 GLOBWB, JULES, LISFLOOD, ORCHIDEE, WaterGAP3, and W3 were used, whereas
182 SURFEX outputs were not used due to incompatibility with the CaMa-Flood hydrodynamic
183 model. In total, 18 ensembles were generated from the runoff outputs of six LSMs/GHMs. We
184 also took variation in meteorological forcing into account; this was assumed normally distributed,
185 with mean = 0 and standard deviation = 0.1 considering the variability of runoffs from twentieth-
186 century atmospheric model ensemble (ERA-20CM: Hersbach et al., 2015). We generated three
187 perturbations from each runoff output. Therefore, there were 18 ensembles in total. Further
188 information regarding runoff forcing is provided in the Supplementary Information (Text S1, Table
189 S1).

190 **2.4 Data assimilation using the LETKF**

191 For the data assimilation method, we used the LETKF (Hunt et al., 2007), which is a
192 variation of the EnKF (Evensen, 2003), an advanced Kalman filter (KF; Kalman, 1960). KF
193 methods estimate future states in time-evolution models by merging model estimates and
194 observations and using weighting procedures that are assessed for their reliability; here, the
195 weighting process is called the Kalman gain. As repeated assimilations progress, better estimates
196 can be made due to the accrual of previous observations. In addition, KF methods assimilate
197 observations and model forecasts using the covariance among pixels. Consequently, a single target
198 pixel is assimilated by combining observations from many pixels. This reduces the likelihood of
199 observation error and also allows locations with no observations to be assimilated. However, KF
200 methods were developed for linear models and cannot be applied to nonlinear models, such as
201 river hydrodynamics models. The EnKF is a variant of the KF that incorporates the Monte Carlo
202 method, enabling data assimilation for nonlinear models. The EnKF calculates different
203 assimilated states using slightly different inputs or initial values. Each of these states is called an
204 ‘ensemble member’ and the set of these members is the ‘ensemble’. The Kalman gain matrix can
205 be calculated from model estimates, even for nonlinear models, using the variation among
206 ensemble members. However, using the EnKF or other KF variants for data assimilation on a
207 global scale is associated with a significant increase in computational cost. Therefore, applying
208 these data assimilation methods to large regions is problematic.

209 The computational cost associated with using the EnKF can be reduced by using the
210 LETKF. This allows data to be assimilated on a global scale. The LETKF is a type of EnKF that
211 increases computational speed by ignoring the covariance between distant pixels (see Text S2 for
212 a detailed description of the LETKF). For each target pixel, a small group of pixels called a ‘local

213 patch' is considered. The Kalman gain matrix for each target pixel is calculated using observation
 214 error and the ensemble variation of forecasted states of the pixels in each local patch. Revel et al.
 215 (2019) developed physically-based adaptive empirical local patches for hydrological data
 216 assimilation that include spatial correlation among the WSE measurements. Further information
 217 regarding empirical local patches is provided in the Supplementary Information (Text S3).

218 We assimilated WSE measurements from SWOT observations into a forecasted water state
 219 using the LETKF (Figure 2) and corrected the initial condition for the next step. For pixels that
 220 had no observations within their local patch, the ensemble of forecasted states was used as the
 221 corrected state. Note that using the LETKF assimilation algorithm may result in mass balance
 222 errors when the local patches are smaller, particularly in upstream river reaches. However,
 223 applying the physically-based adaptive empirical local patch considerably decreases mass balance
 224 errors. Previous water states were not corrected in the current time step, which may have resulted
 225 in mass balance errors. Implementing smoothing data assimilation methods, such as the Kalman
 226 smoother, can reduce these errors. However, this greatly increases the computational cost and may
 227 raise new uncertainties. Our focus was to provide better river discharge estimates on a global scale.
 228 We do not recommend that the outputs from this study are used for precise mass balance
 229 calculations. The major advantage of using the LETKF assimilation here was its increased
 230 computational speed.

231 **3. Evaluation of the Data Assimilation Framework**

232 **3.1 Experimental objectives and assumptions**

233 We performed OSSEs to evaluate the river discharge estimates from the SWOT data
 234 assimilation framework. OSSEs are often used to assess the potential of new measurements before
 235 these are implemented (Sylvain Biancamaria et al., 2016). In the OSSEs, we generated synthetic
 236 observations using a hydrodynamic model and compared them with the assimilated results. The
 237 OSSEs consisted of three parts: the 'true simulation' representing the assumed-to-be-true
 238 (hereafter true) situation to generate synthetic SWOT observations for data assimilation; the
 239 'corrupted simulation' representing a model forecasted simulation, which is usually separate from
 240 the true state; and the 'assimilated simulation' representing data assimilation from a model forecast
 241 using synthetic SWOT observations (Figure 2). The object of these experiments was to evaluate
 242 our SWOT data assimilation framework and determine whether it can estimate global river
 243 discharge accurately with poor land surface runoff forcing data and/or poor model parameter
 244 estimates. We made the following assumptions for these experiments:

- 245 1. We assumed similar models may be used to generate virtual SWOT observations and
 246 forecasted water states. We used the CaMa-Flood hydrodynamic model to represent both true
 247 and corrupted/assimilated water states. However, the CaMa-Flood model includes
 248 uncertainties in both its physics and model parameters. For example, the CaMa-Flood model
 249 assumes that WSE measurements for the river channel and floodplain are the same within each
 250 grid box, whereas observation-based studies have suggested that there is a time lag in water-
 251 level changes between these two situations (Alsdorf et al., 2005). A uniform water level was
 252 assumed for each 0.25° pixel, whereas real WSEs have sub-grid variations. In addition,
 253 incorrect topography parameters (e.g., elevation and channel bathymetry) will generate bias in
 254 water state forecasts. The CaMa-Flood model uses a global constant value for Manning's
 255 coefficient, although these are spatially distinct. Due to the uncertainties described above,
 256 using the same hydrodynamic model for true and corrupted/assimilated simulations in OSSEs

257 may be too optimistic because the hydrodynamics of actual rivers may not well represent in
 258 hydrodynamic models. Therefore, we also assessed imperfect model conditions, which are
 259 represented by using different Manning's coefficients in true and corrupted/assimilated
 260 simulations in this study. Further information regarding the imperfect model experiment is
 261 provided in section 3.4.

262 2. We assumed that synthetic SWOT observations are compatible with the CaMa-Flood model-
 263 grid scale (~25 km). The SWOT satellite will observe WSE at 50–100 m resolution, depending
 264 on the distance from the satellite (Fjørtoft *et al.*, 2014). Therefore, it is necessary to increase
 265 the scale of high-resolution SWOT observations to match the coarse-scale grids of the CaMa-
 266 Flood model. This is particularly important in steep river reaches and areas with floodplains,
 267 where sub-grid variations in WSE are large. Consequently, the mean WSE cannot be used in
 268 the coarse-scale grid for data assimilation under the unit-catchment assumption of the CaMa-
 269 Flood model (Yamazaki *et al.*, 2011). Therefore, we assumed that average SWOT observations
 270 within a certain distance of the unit-catchment mouth can be used for data assimilation in this
 271 study. Further information on generating synthetic SWOT observations is provided in section
 272 3.2.1.

273 3. We also assumed that the SWOT satellite can measure the WSE of rivers > 50 m in width at
 274 10 cm error (water area ≥ 1 km²) accuracy (25 cm for [250 m]²; water area < 1 km²). These
 275 thresholds were adopted in accordance with the mission goal (Desai *et al.*, 2018) and estimated
 276 error limits of the SWOT satellite mission (Esteban-Fernandez, 2017). Further information on
 277 generating synthetic SWOT observations from these assumptions is provided in section 3.2.
 278 The observation capability for each river grid is complex and varies with river width, river
 279 length, surrounding topography (Durand *et al.*, 2010), and distance from the satellite track
 280 (varies between 4~10cm) (Esteban-Fernandez, 2017).

281 3.2 Experimental design

282 3.2.1 Overview of OSSEs

283 The workflow for the OSSEs is shown in the Figure 2. We performed three simulations:
 284 'true', 'assimilated', and 'corrupted'. From the true simulation we derived the synthetic SWOT
 285 observations. In the assimilated simulation, we tested our assimilation framework, and we used
 286 the corrupted simulation to evaluate our data assimilation framework. We performed the OSSEs
 287 over a 1-year period from 1 January 2004 to 31 December 2004. A 1-year spin-up simulation was
 288 used to generate initial conditions for the true and corrupted/assimilated simulations.

289 We used the 'true simulation' to generate the true water state, which was continuous in
 290 space and time. In the true simulation, the hydrodynamic model was forced by true input runoff
 291 (i.e., HTESSSEL LSM runoff output from E2O WRR2), generating the true water state (e.g., river
 292 discharge, WSE, and water storage). The initial condition for the true simulation was prepared
 293 using a spin-up simulation with the same model settings. The true simulation was used to generate
 294 the synthetic SWOT observations and to evaluate the results of assimilation.

295 To evaluate the assimilation framework, we performed the 'corrupted simulation'. The
 296 modified LSM runoff outputs (representing uncertainty in the meteorological data) from E2O
 297 WRR2 were used in the corrupted simulation. We used the standard global value of 0.03 for
 298 Manning's coefficient (Yamazaki *et al.*, 2011). Using similar input runoffs and model parameters,
 299 the water state at the beginning of the simulation period (2004) was prepared by running the CaMa-

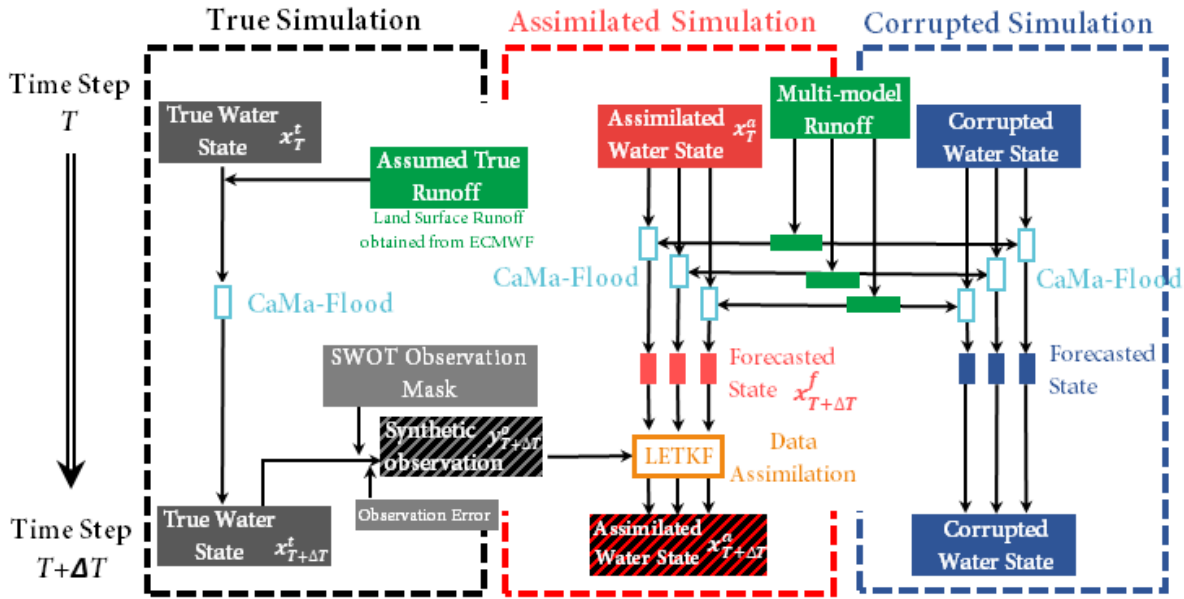


Figure 2: Workflow for the virtual experiment

300 Flood model for 1 year (2003). The data assimilation procedure was not implemented for the
 301 corrupted simulation.

302 Next, we performed the ‘assimilated simulation’ to evaluate the use of SWOT observations
 303 in estimating global river discharge. We used the same model settings and inputs that were used
 304 for the corrupted simulation, but the water state was corrected by assimilating synthetic SWOT
 305 observations. We used a physically-based data assimilation technique (Revel et al., 2019) based
 306 on the LETKF data assimilation algorithm, as described in section 2.4.

307 3.2.2 Synthetic SWOT observations

308 Synthetic SWOT observations were generated by overlaying the SWOT coverage mask
 309 onto WSE measurements from the true simulation (Figure 3a). Therefore, we assumed that only
 310 part of the true water state (i.e., WSE measurements from SWOT observations) was known, as
 311 would be the case if real SWOT satellite observations were being used. The SWOT coverage mask
 312 was created using SWOT orbit data (Figure 3a, center panel) available online at the Centre national
 313 d’études spatiales web page (CNES, 2015). The orbit data indicate the satellite’s path of the 120
 314 km wide observation swath with a 20 km nadir gap for each day, for 21-day orbit cycle. The SWOT
 315 coverage mask was created at a resolution of 0.25° to match the grid coordination system of the
 316 CaMa-Flood model. If the center of each 0.25° grid was within the observation range of the path
 317 data, the grid was considered observed. Because the observed area was different for each day of
 318 the orbit cycle, we prepared 21 coverage masks to generate synthetic SWOT observations. Rivers
 319 wider than 50 m and within the coverage mask (Figure 3a, right panel) were considered as
 320 observed. We also included observation error in the synthetic observations to represent
 321 measurement errors. We simulated SWOT observation errors using a mean value of zero and
 322 standard deviation of 10 cm, in accordance with the SWOT mission goal of measurement accuracy
 323 (Desai et al., 2018; Esteban-Fernandez, 2017). We modeled the measurement error h_{err} as follows:

$$h_{err} = N\left(0, \frac{1}{WL} \sigma_h\right) \quad (1)$$

324 where W is the river width and L is the river length. In this study, L was set to 1 km to include only
 325 observations near the unit catchment mouth, due to internal variation inside the unit-catchment in
 326 the CaMa-Flood hydrodynamic model. The term σ_h represents observation error, as described in
 327 the SWOT mission goal (Desai et al., 2018; Esteban-Fernandez, 2017), and is equivalent to 10 cm
 328 for a water area ≥ 1 km² and 25 cm for 1 km² > water area ≥ 0.625 km². The observation error
 329 variance is illustrated in Figure S1 and described in Text S4.

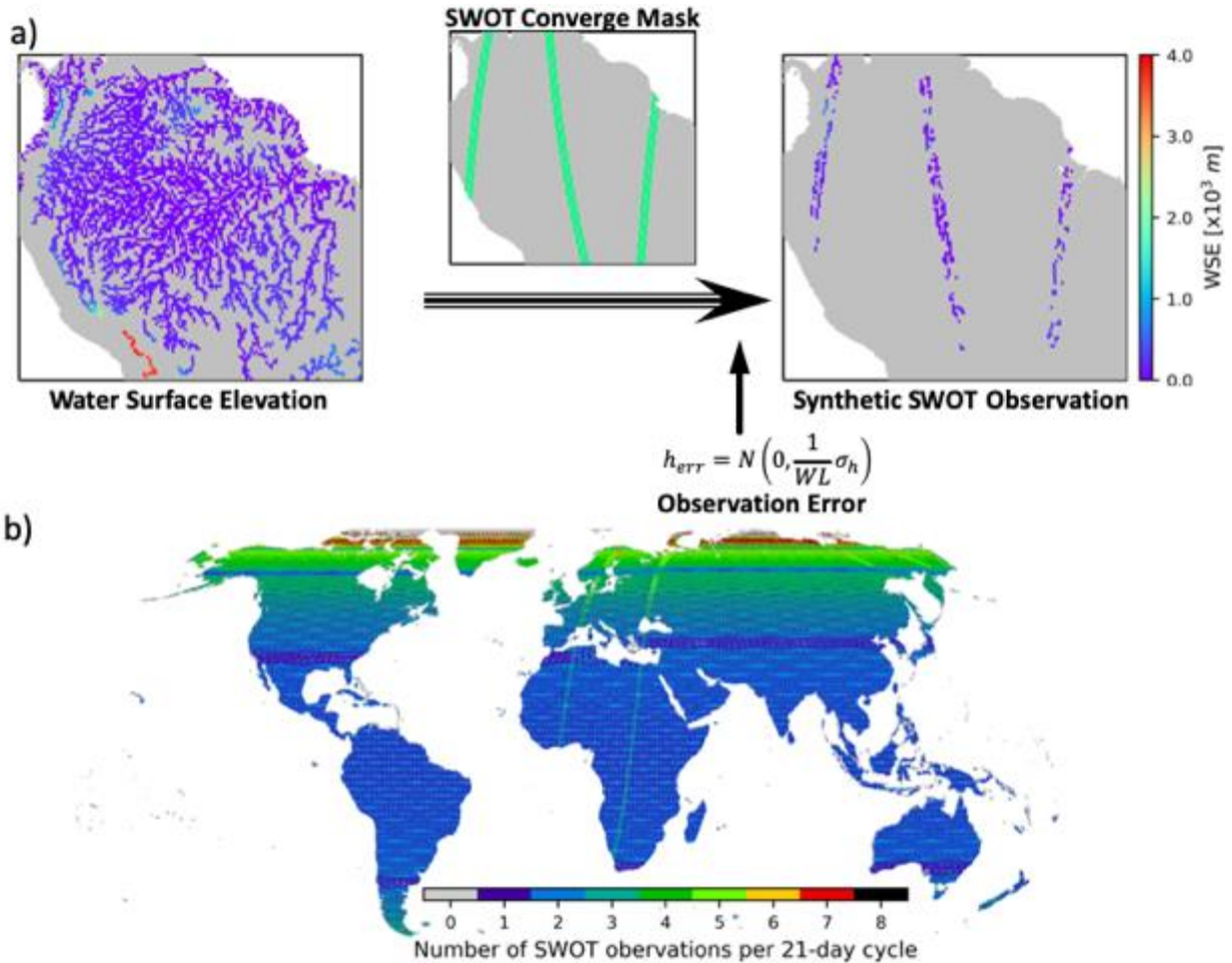


Figure 3: Generation of synthetic SWOT observations. (a) True water surface elevation (left), SWOT coverage mask (center), and synthetic observations (right). (b) Number of SWOT observations within the 21-day cycle. Only ground observations are shown.

320 3.2.3 Experimental conditions

331 We performed two experiments with different model settings: perfect and imperfect. The
 332 experimental conditions are summarized in Table 1. The perfect model experiment included errors
 333 in input runoff forcing, whereas model errors and unrealistic forcing were assumed in the imperfect
 334 model experiment.

Table 1: Experimental conditions, including experiment name, Manning’s coefficient conditions for true and corrupted /assimilated simulations, as well as input runoff forcing for true and corrupted /assimilated simulations.

<i>Experiment</i>	<i>Simulation</i>	<i>Manning’s Coefficient</i>	<i>Input Runoff Forcing</i>
<i>Perfect model experiment</i>	True	Global Constant (0.030)	Runoff forcing from HTESSEL LSM
	Corrupted	Global Constant (0.030)	Modified Ensemble runoff from E2O LSM/GHMs
	Assimilated	Global Constant (0.030)	Modified Ensemble runoff from E2O LSM/GHM s
<i>Imperfect model experiment</i>	True	Spatially varied value depends on the river width	Runoff forcing from HTESSEL LSM
	Corrupted	Global Constant (0.030)	Modified Ensemble runoff from E2O LSM/GHMs
	Assimilated	Global Constant (0.030)	Modified Ensemble runoff from E2O LSM/GHMs

335 **a) Perfect model experiment**

336 To assess the effectiveness of assimilation when a good model is available, we performed
 337 a ‘perfect’ model experiment in which we assumed that there were no errors in the hydrodynamic
 338 model. In this experiment, we used the same model parameters (e.g., Manning’s coefficient, river
 339 channel depth, and river width) for all three simulations. However, the input runoff forcing for true
 340 and corrupted/assimilated simulations had different runoff inputs from different LSMs/GHMs.

341 **b) Imperfect model experiment**

342 We also performed an experiment to evaluate river discharge estimates obtained using
 343 data assimilation under erroneous model conditions, because modeled river states differ from those
 344 of real rivers due to uncertainties in the model physics and parameters. In this experiment, the
 345 corrupted/assimilated simulation was performed using a global constant value for Manning’s
 346 coefficient and corrupted input runoff forcing. We assumed the model error can be represented
 347 using the error of the Manning’s coefficient values in the hydrodynamic model due the large
 348 uncertainty in estimating true Manning’s coefficients. To represent model uncertainty, we used
 349 different Manning’s coefficients for the true and corrupted simulations. For the true simulation,
 350 we used a different value for each pixel, depending on the river width. We used a constant value
 351 of 0.030 for all river pixels in the corrupted and assimilated simulations. The spatially distributed
 352 Manning’s coefficient for the true simulation was modeled as described by (Pedinotti et al., 2014),
 353 as shown below:

$$n = n_{min} + (n_{max} - n_{min}) \left(\frac{W_{max} - W}{W_{max} - W_{min}} \right) \quad (2)$$

354 where n is the unit catchment average Manning's coefficient at river width W . n_{max} and n_{min} are
 355 maximum and minimum Manning's coefficients, which are 0.025 and 0.035, respectively. W_{max}
 356 and W_{min} are the maximum and minimum river widths for the river basin in the MERIT hydro
 357 river network map (Yamazaki et al., 2019). Figure 4 shows the spatial distribution of Manning's
 358 coefficient, modeled using equation (2). Relatively small upstream river sections have relatively
 359 large Manning's coefficient values (≈ 0.035), whereas relatively large downstream river sections
 360 have relatively small Manning's coefficient values (≈ 0.025). In this study, we ignored the
 361 uncertainties associated with the model physics to reduce the complexity of the data assimilation
 362 framework.

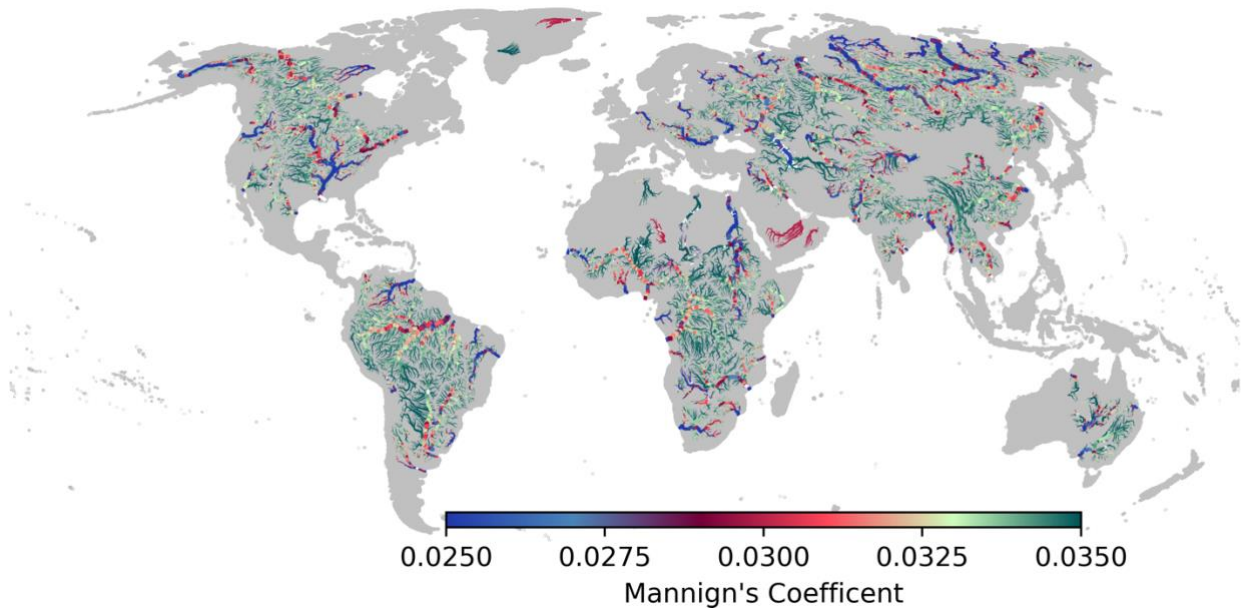


Figure 4: Spatially distributed Manning's coefficient modelled using the equation (2).

363 3.3 Assimilation diagnostics

364 The effectiveness of the data assimilation framework was evaluated by comparing the
 365 assimilated water state and the true water state. If these two water states were similar, the
 366 assimilation framework was considered effective. However, if the assimilated water state was
 367 similar to the corrupted water state, then the assimilation framework had not significantly
 368 improved river discharge estimates. We used several indices to evaluate the effectiveness of the
 369 assimilation framework. The 'assimilation index' (AI) was used to evaluate the instantaneous
 370 effect of assimilation on a daily timescale. The Nash–Sutcliffe efficiency (NSE; Nash & Sutcliffe,
 371 1970) based AI (NSEAI) was used to evaluate the effectiveness of assimilation over the entire
 372 simulation period of 366 days. In addition, the Kling-Gupta efficiency (KGE; Gupta et al., 2009;
 373 Kling et al., 2012), which is often used to evaluate model results against observations, was used to
 374 measure the accuracy of assimilated river discharge estimates. AI and NSEAI were used to assess
 375 improvements in assimilated river discharge compared to that of true and corrupted simulation

376 results, whereas the KGE was used to evaluate the expected accuracy of assimilated river discharge
377 estimates.

378 **3.3.1 Assimilation index**

379 We introduced a new metric, the AI, to evaluate the effectiveness of data assimilation in a
380 virtual experiment. The AI was calculated from the ratio of instantaneous river discharge error
381 rates in the assimilated and corrupted simulations using equation (3):

$$AI = 1 - \left| \frac{Q_T - Q_A}{Q_T - Q_C} \right| \quad (3)$$

382 where Q_T , Q_A , and Q_C represent daily discharge from true, assimilated, and corrupted simulations,
383 respectively. Here, Q_A and Q_C represent the mean discharge from ensemble members in each
384 simulation.

385 The AI describes the similarity between the assimilated and true simulations, compared to
386 the similarity between the corrupted and true simulations. A high AI (maximum of 1) indicates
387 that the assimilated discharge estimate is close to the true discharge, whereas a low AI indicates
388 that the assimilated discharge estimate is not significantly better than the corrupted discharge
389 estimate. An AI value of less than zero indicates that the assimilated simulation includes more
390 error than the corrupted simulation. The AI represents the relative effectiveness of data
391 assimilation and, in contrast to the NSE coefficient (Nash & Sutcliffe, 1970), is not a measure of
392 simulation accuracy. In addition, the AI can be calculated for any time and location during the
393 experiment. Consequently, we can potentially identify when and where the data assimilation
394 framework was effective in estimating river discharge. Therefore, the AI may be used to evaluate
395 the instantaneous effects of our data assimilation strategy.

396 **3.3.2 Nash–Sutcliffe efficiency-based assimilation index**

397 The NSEAI was also calculated to evaluate the effectiveness of assimilation, because when
398 the results of the corrupted and true simulations are similar, the AI may not provide the best
399 assessment of assimilation effectiveness. The NSEAI was calculated by comparing the difference
400 between the NSE values for assimilated and corrupted simulations, as in equation (4):

$$NSEAI = \frac{NS_A - NS_C}{1 - NS_C} \quad (4)$$

402 where NS_A and NS_C are the NS coefficients for the assimilated and corrupted simulations,
403 respectively. The relative difference between the accuracy of these two simulations is given by
404 equation (4). The NSEAI represents the overall effectiveness of assimilation over the entire
405 simulation period. The NSEAI avoids any over-evaluation that may be due to the corrupted
406 simulation coinciding with the true simulation.

407 **3.3.3 Kling–Gupta efficiency**

408 We used the KGE to compare the accuracy of the assimilated and corrupted simulations.
409 The KGE is an integrated skill metric which is based on a combination of three diagnostically
410 meaningful components of the mean squared error. The mean squared error for the simulated and
411 observed discharge can be separated into three components including the mean, variability, and

412 dynamics (Gupta et al., 2009). These components can be represented by the correlation coefficient
 413 (CC), bias ratio (BR), and relative variability (RV). The KEG is given by equation (5):

$$414 \quad KGE = 1 - \sqrt{(CC - 1)^2 + (BR - 1)^2 + (RV - 1)^2} \quad (5)$$

415 where;

$$CC = \frac{cov(Q_m, Q_o)}{\sigma_{Q_m} \sigma_{Q_o}} \quad (6)$$

$$BR = \frac{\mu_{Q_m}}{\mu_{Q_o}} \quad (7)$$

$$RV = \frac{\left(\frac{\sigma_{Q_m}}{\mu_{Q_m}}\right)}{\left(\frac{\sigma_{Q_o}}{\mu_{Q_o}}\right)} \quad (8)$$

416 where Q , μ , and σ are the discharges, the mean of the discharges, and the standard deviation of the
 417 discharges, respectively. The subscripts m and o represent the simulated (assimilated/corrupted)
 418 and true discharges, respectively. In addition, conventional metrics, such as the percent bias
 419 (pBias) of annual mean river discharge, were also used in our evaluations.

420 **4. Results**

421 **4.1 Perfect model experiment**

422 Here, we describe the results of the perfect model experiment. First, we evaluated the
 423 results obtained for the Amazon basin, the world's largest river basin, to assess the effectiveness
 424 of our data assimilation framework in river discharge estimates for continental-scale rivers. Next,
 425 we evaluated the potential effectiveness of SWOT observations in river discharge estimates on a
 426 global scale.

427 **4.1.1 Amazon River basin**

428 Figure 5a–c shows the temporal variation in simulated river discharge at three locations on
 429 the Amazon River: upstream location X (1.125°S, 74.875°W), midstream location
 430 Y (1.625°S, 67.625°W), and downstream location Z (0.875°S, 51.125°W), respectively. Black, blue,
 431 and red lines represent the discharge for the true, corrupted, and assimilated simulations,
 432 respectively. The green lines illustrate the temporal variation in AI defined by equation (3). The
 433 AI is marked only for those days in which the true and corrupted discharge showed significant
 434 error (>5%) because the AI is much lower, despite the effectiveness of the assimilation, when the
 435 two discharges are similar. Green circles indicate the days when the assimilation was performed
 436 at each location. In addition, the NSEAI and the transition of the annual mean pBias from a
 437 corrupted to an assimilated value is shown in the top right corner of the graph.

438 At downstream location Z, the assimilated discharge was almost identical to the true
 439 discharge, although the initial conditions were generated using corrupted runoff. The AI at location
 440 Z remained >0.8 during most of the simulation period and was generally stable, regardless of
 441 SWOT assimilation availability. There were some low AI values when the discharge error between

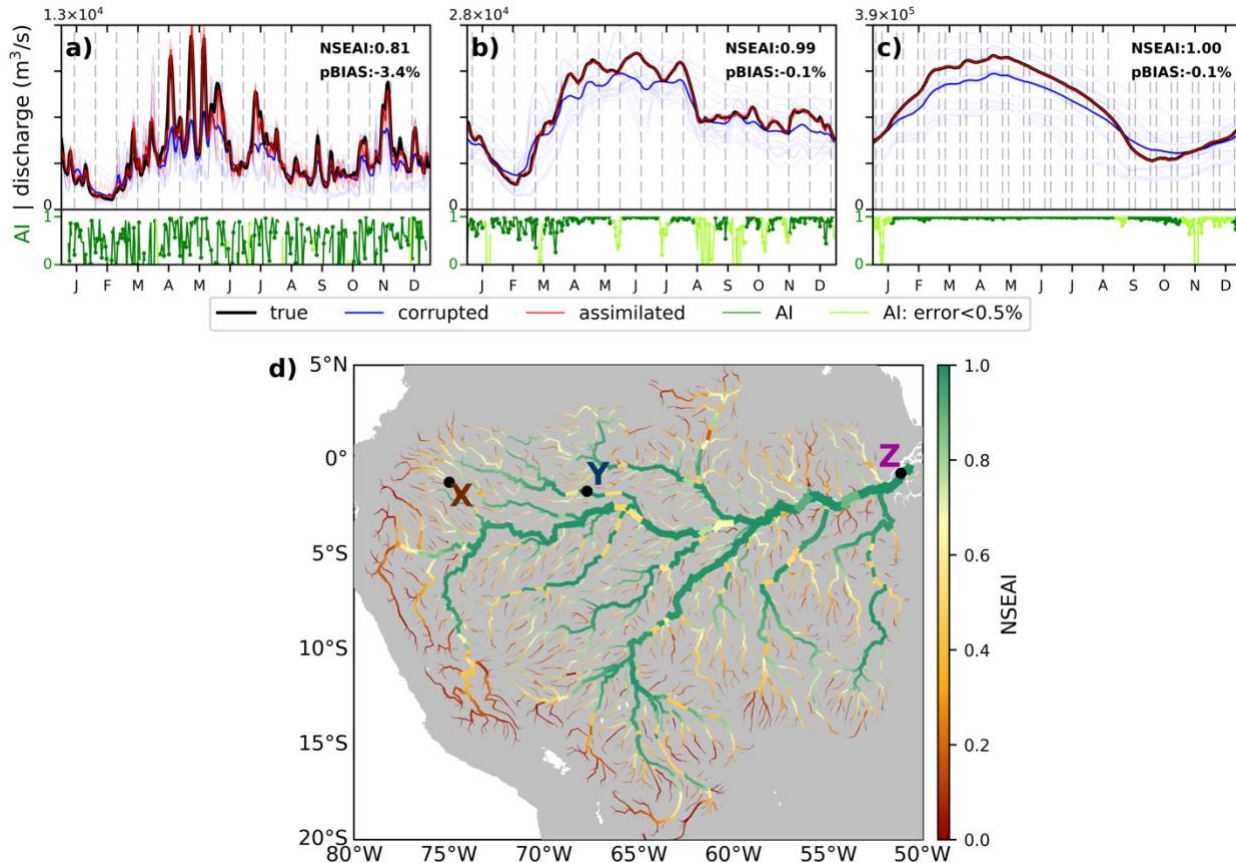


Figure 5 : Simulated river discharge and Nash-Sutcliffe efficiency-based assimilation index (NSEAI) in the Amazon basin. Discharge hydrographs at the a) upstream X(1.125°S,74.875°W), b) midstream Y(1.625°S,67.875°W), and c) downstream Z(0.625°S,51.125°W). River discharges of true, assimilated, and corrupted simulations are shown by black, red, and light blue lines, respectively. Dark blue line represents the ensemble mean of corrupted simulation. The dashed-grey vertical lines indicate the times of direct SWOT observations. The assimilation index (AI) (green line in lower panel) is shown for days when the error between the true and corrupted discharges was $>5\%$. Light green line indicates the AI when error was $<5\%$. Green dots represent the times of data assimilation. The NSEAI and percent bias (pBIAS) of the assimilated simulation are shown in the upper right corner of the hydrographs. (b) map of NSEAI. The locations of hydrographs X, Y, and Z are annotated by black dots.

442 the true and corrupted simulations was $<5\%$ in Figure 5c. At the upstream location X, the overall
 443 trend for discharge in the assimilated simulation was similar to that observed for the true simulation
 444 (Figure 5a). However, the difference between the two discharges was unstable and varied
 445 throughout the year. In addition, AI values fluctuated significantly and were frequently large on
 446 assimilation days (i.e., days with green circles on the AI graph) but small thereafter. At the
 447 midstream location Y (Figure 5b), discharge in the assimilated simulation generally matched true
 448 discharge, as it did at downstream location Z. However, fluctuations observed at location Y were
 449 greater than those observed at location Z. The NSEAI value was greatest at location Z and lowest
 450 at upstream location X. The NSEAI value at location Y was intermediate.

451 Figure 5d shows the spatial distribution of NSEAI values throughout the Amazon basin.
 452 The NSEAI was calculated for each grid to compare the effectiveness of data assimilation at

453 different locations. Because the runoff error varied over time, AI values also fluctuated. Therefore,
454 the level of agreement among overall discharge values for true and assimilated simulations also
455 varied over time. To obtain the overall discharge correction, we developed the NSEAI (equation
456 4) to evaluate the effectiveness of assimilation. At downstream location Z, the NSEAI value was
457 greater (1.00) than at upstream location X (0.98) or midstream location Y (0.78). The Amazon
458 basin and associated river branches (i.e., the Amazon, Solimoes, and Madeira Rivers) had high
459 NSEAI values (> 0.8), indicating effective assimilation. Other large river branches (e.g., the
460 Tapajos, Negro, Purus, Juura, and Paura Rivers) also had relatively high NSEAI values (> 0.6),
461 whereas most minor river branches had lower NSEAI values (< 0.4). These results imply that
462 SWOT data assimilation is more effective at improving river discharge estimates in large rivers
463 than in upstream river reaches.

464 NSEAI values were strongly influenced by two factors: the local state correction and the
465 upstream inflow correction. Local state correction is a water state update derived from SWOT data
466 assimilation at the current location. This is a direct correction based on SWOT observations and
467 occurs only when a SWOT observation is available within its' local patch. Local state corrections
468 were available only once every few days, particularly for upstream river reaches, because the
469 empirical local patches were not large enough to accommodate SWOT observations every day.
470 The effects of local state corrections were most obvious at upstream location X (Figure 5a). Here,
471 the AI rapidly increased when local SWOT observation assimilations occurred (green circles,
472 Figure 5a) Local state corrections were effective at locations where the river water flow from
473 upstream was less than the surface and subsurface runoff. At these pixels, the variation among the
474 ensemble is likely to increase rapidly because the water state is sensitive to a change in external
475 conditions (e.g., runoff forcing). This increase in ensemble variation affected the Kalman gain
476 matrix and decreased model weight while increasing observation weight at data assimilation. In
477 addition, at these pixels, river discharge differences between the assimilated and true simulations
478 increased when assimilation was unavailable because the water state is sensitive to surface and
479 subsurface runoff and river discharge fluctuates frequently. Therefore, AI values decreased when
480 assimilation was unavailable.

481 The second factor strongly influencing NSEAI values, upstream inflow correction, is
482 caused by previously corrected water states from upstream pixels. Downstream pixels are more
483 accurate when the water state at upstream pixels is corrected, because the upstream water state
484 significantly affects river discharge at downstream locations. This factor is independent of local
485 SWOT observation availability because it has an indirect effect on local data assimilation. The
486 upstream inflow correction was significant at downstream location Z (Figure 5c). Here, AI values
487 remained high (mean AI= 0.96) and the NSEAI reached its maximum value (i.e., 1.00) because
488 the upstream drainage area at this location is large. Consequently, upstream inflow correction was
489 constantly available somewhere within the catchment area. AI values did not fluctuate as much at
490 location Z as they did at locations X or Y. Local state and upstream inflow corrections were both
491 significant factors at midstream location Y (Figure 5b). Upstream inflow correction was observed
492 as increased AI values on days on which no local observations were recorded. However, the AI
493 values showed some fluctuations due to the smaller drainage area at location Y, compared to that
494 at downstream location Z. The increases in AI values at location Y, which were due to local state
495 corrections, were smaller than those observed at upstream location X. At location Y, the
496 combination of upstream inflow and local state corrections meant that the NSEAI was high (0.98).
497 At upstream location X, the upstream inflow correction was smaller and AI values generally
498 increased at the days of assimilation. At location X, the catchment area was smaller (44916.08

499 km²) than at locations Y or Z, and location X also had a smaller upstream river reach (width > 50
 500 m) where SWOT observations could be made. Therefore, at location X, there was a lower
 501 probability of inflow assimilation upstream, which limited the effect of inflow corrections. To
 502 evaluate the importance of upstream inflow corrections further, we performed an extra experiment
 503 in which upstream inflow corrections were excluded (Text S5 and Figure S2). We found that AI
 504 values significantly decreased when upstream inflow corrections were excluded, suggesting that
 505 data assimilation must be applied to the entire upstream region to estimate discharge in a large
 506 basin accurately.

507 Figure 6 shows the percentage deviation from true value (pBias) of annual river discharge
 508 for the assimilated (Figure 6a) and corrupted (Figure 6b) simulations compared to the true
 509 simulation. As with the NSEAI values (Figure 5d), the annual mean river discharge was accurately
 510 estimated in the major branches of the Amazon River. The pBias of the assimilated river discharge
 511 was almost zero, particularly in the downstream reaches of the Amazon mainstream (50–65°W),
 512 which indicates that the virtual assimilation framework succeeded in accurately estimating the total
 513 quantity of water flowing from the Amazon basin to the Atlantic Ocean. These results are
 514 promising because estimates for the terrestrial water budget within the global hydrological cycle
 515 are generally unreliable where sparse distribution of river gauges makes it difficult to estimate the
 516 total freshwater discharge from land to the oceans.

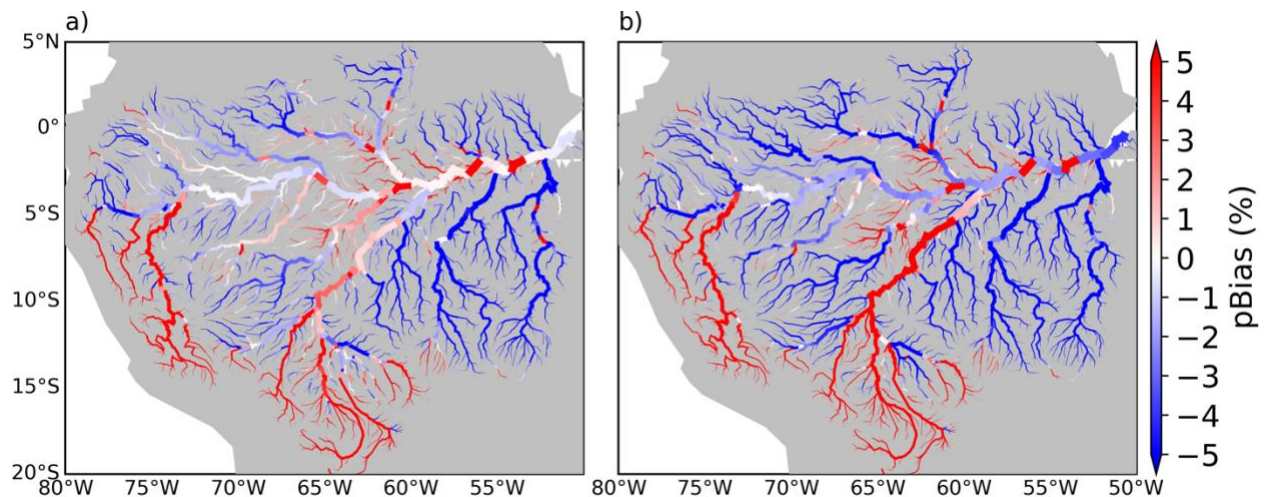


Figure 6 : Percentage bias (pBias) of river discharge in Amazon basin: a) between the assimilated and true simulations (left), and b) between the corrupted and true simulations (right).

517 4.1.2 Global-scale analysis

518 Figure 7 shows simulated river discharge hydrographs for 42 locations, which are also
 519 listed in Table 2. Table 2 describes the geographical details and assimilation diagnostics of each
 520 location. We selected three locations for each river: upstream, midstream, and downstream. Each
 521 row of panels in Figure 7 represents one river (e.g., row 1 of Figure 7 shows the hydrographs for
 522 the Amazon River: upstream, midstream, and downstream from left to right, respectively). In
 523 addition, the geographical location of each hydrograph is marked in Figure 8. The locations are
 524 indicated by two upper-case characters in the upper-left corner of each panel in Figure 7 (e.g., PK
 525 = Prek Kadam). Furthermore, NSEAI values and the pBias of the assimilated simulation are shown
 526 in the upper-left corner of each panel (in the PK panel, these are shown upper center). We

527 deliberately included PK, which is not on the main stream of the Mekong River but situated
528 between the Tonlè Sap and the Mekong, to discuss the effectiveness of our assimilation framework
529 in scenarios involving reverse flow.

530 Generally, the distribution of NSEAI values was similar to that observed in the Amazon
531 River basin, with high NSEAI values downstream and low values upstream. Among the 14 rivers
532 shown in Figure 7, the Amazon, Ob, Lena, Mississippi, Volga, Ganges–Brahmaputra, Nile,
533 Yangtze, Yukon, Indus, and Irrawaddy generally had higher NSEAI values downstream than
534 upstream. For the Congo River, the Kinshasa (KH) location had a slightly lower NSEAI value
535 (0.74) than upstream locations due to the corrupted simulation result, which was very similar to
536 the true simulation. Similarly, for the Niger River, the downstream Lokoja (LJ) location had a
537 slightly lower NSEAI value (0.93) than upstream locations. In addition, PK had a high NSEAI
538 value (0.97) although PK is not on the main stream of the Mekong River. Most of the other
539 hydrographs shown in Figure 7 had higher NSEAI values at downstream than upstream locations.

540 Some important hydrodynamic processes (e.g., reverse flow towards Tonlé Sap in the
541 Mekong River, glacial runoff in the Yukon River, and backwater effects in the Amazon River)
542 were captured using our assimilation framework and the CaMa-Flood hydrodynamic model.
543 Reverse flow towards Tonlé Sap in the wet season was well-characterized by the CaMa-Flood
544 model. In addition, negative discharges at PK (Figure 7) were also well estimated by our data
545 assimilation framework, achieving an NSEAI value of 0.97. Glacier runoff from the Llewellyn
546 Glacier at Atlin Lake is the main source for the Yukon River in Alaska, but in LSMs the glacier
547 runoff process may not be well-characterized (Hock, 1998; Hock & Holmgren, 2005; Zhao et al.,
548 2013). Clearly, the timing of peak flow for the true and corrupted simulations was different. Our
549 data assimilation framework can be used to accurately estimate discharge even if glacier runoff is
550 not modeled successfully (e.g., the Dawson [DW], Stevens Village Ak [SV], and Kaltag, alas.
551 [KA] in Figure 7). The discharge along the main stream of the Amazon River was estimated
552 accurately (NSEAI > 0.99). In addition, hysteresis in the stage–discharge relationship due to
553 backwater effects has also been successfully modeled in the Amazon River using the CaMa-Flood
554 hydrodynamic model (Yamazaki et al., 2012). Because we assimilated the WSE by including
555 SWOT observations, the water-surface dynamics were well-characterized. Therefore, important
556 hydrodynamic processes such as reverse flow, glacier-runoff-induced river discharge, and
557 backwater effects were captured using our assimilation framework and the CaMa-Flood
558 hydrodynamic model.

559 The large lakes and their downstream reaches had relatively low NSEAI values compared
560 to nearby reaches. For the Great Lakes of North America, the NSEAI values were slightly smaller
561 than those of the surrounding river reaches (Figure 8). For such large lakes, the quantity of
562 discharge may be determined from upstream water flow, particularly during the dry season. Due
563 to less rainfall and runoff, the ensemble of forecasted water states is less diverse because the
564 quantity of inflowing runoff is small compared to the total water storage. The small variation in
565 forecasted WSE decreased model variance in the Kalman gain matrix, which hampered data
566 assimilation and decreased NSEAI values. However, lakes situated downstream of these rivers had
567 high NSEAI values due to large upstream inflow correction from upstream reaches. For example,
568 the Caspian Sea, which is situated downstream of the Volga River, had very high NSEAI values.
569 Therefore, upstream river reaches where upstream flow is greater than surface and subsurface
570 runoff showed low assimilation efficiencies, whereas downstream river reaches showed higher
571 assimilation efficiencies.

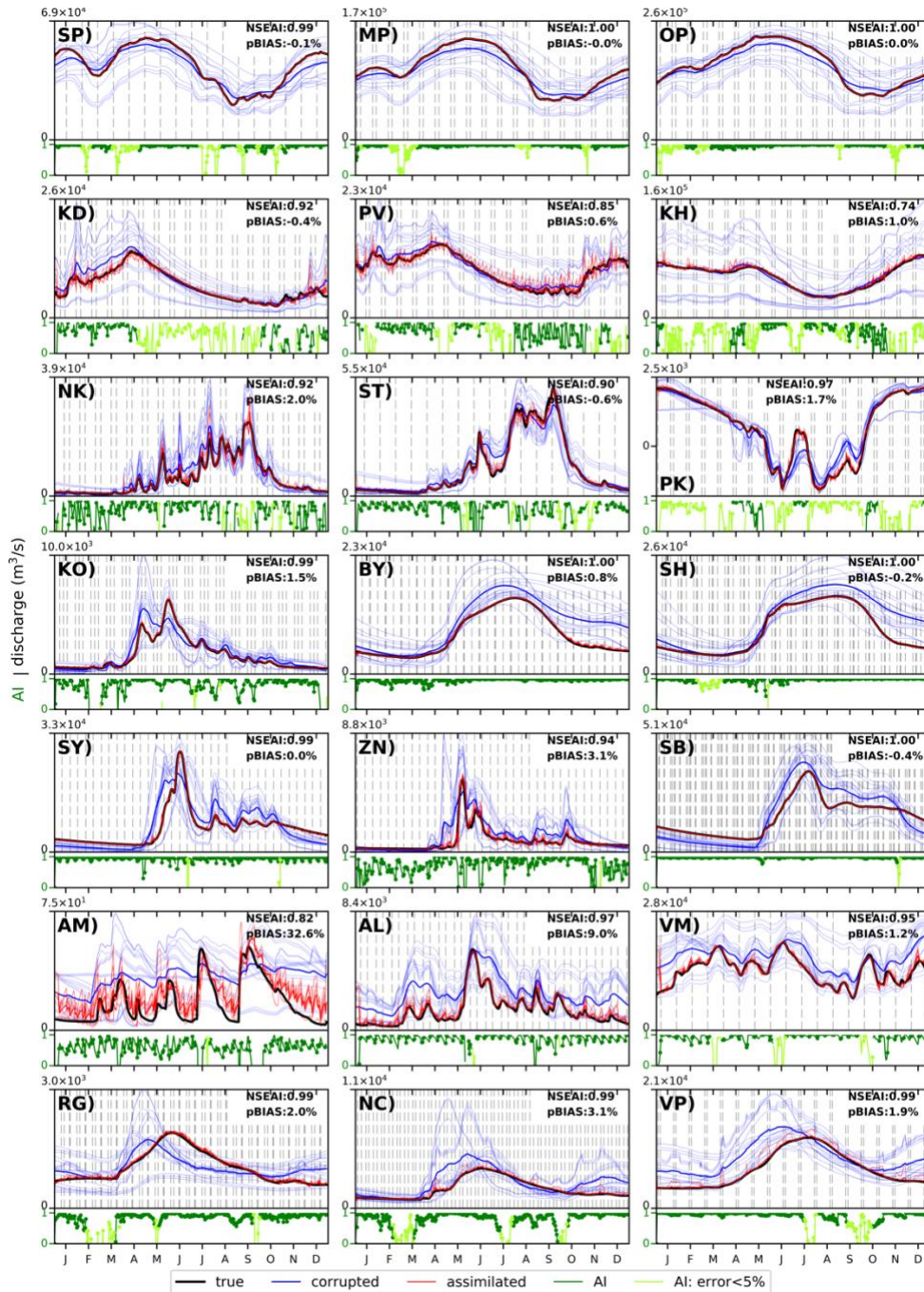


Figure 7 : Simulated discharge for the perfect model experiment on a global scale. The locations are summarized in Table 2. River discharges of true, assimilated, and corrupted simulations are shown by black, red, and light blue lines, respectively. Dark-blue line represent the ensemble mean of corrupted simulation. The dashed-grey vertical lines indicate the times of direct SWOT observations. The assimilation index (AI) (green line in lower panel) is shown for days when the error between the true and corrupted discharges was >5%. Light green line indicates the AI when error < 5%. Green dots represent the times of data assimilation. The colors and key are identical to those shown for Figure 5a-c.

573

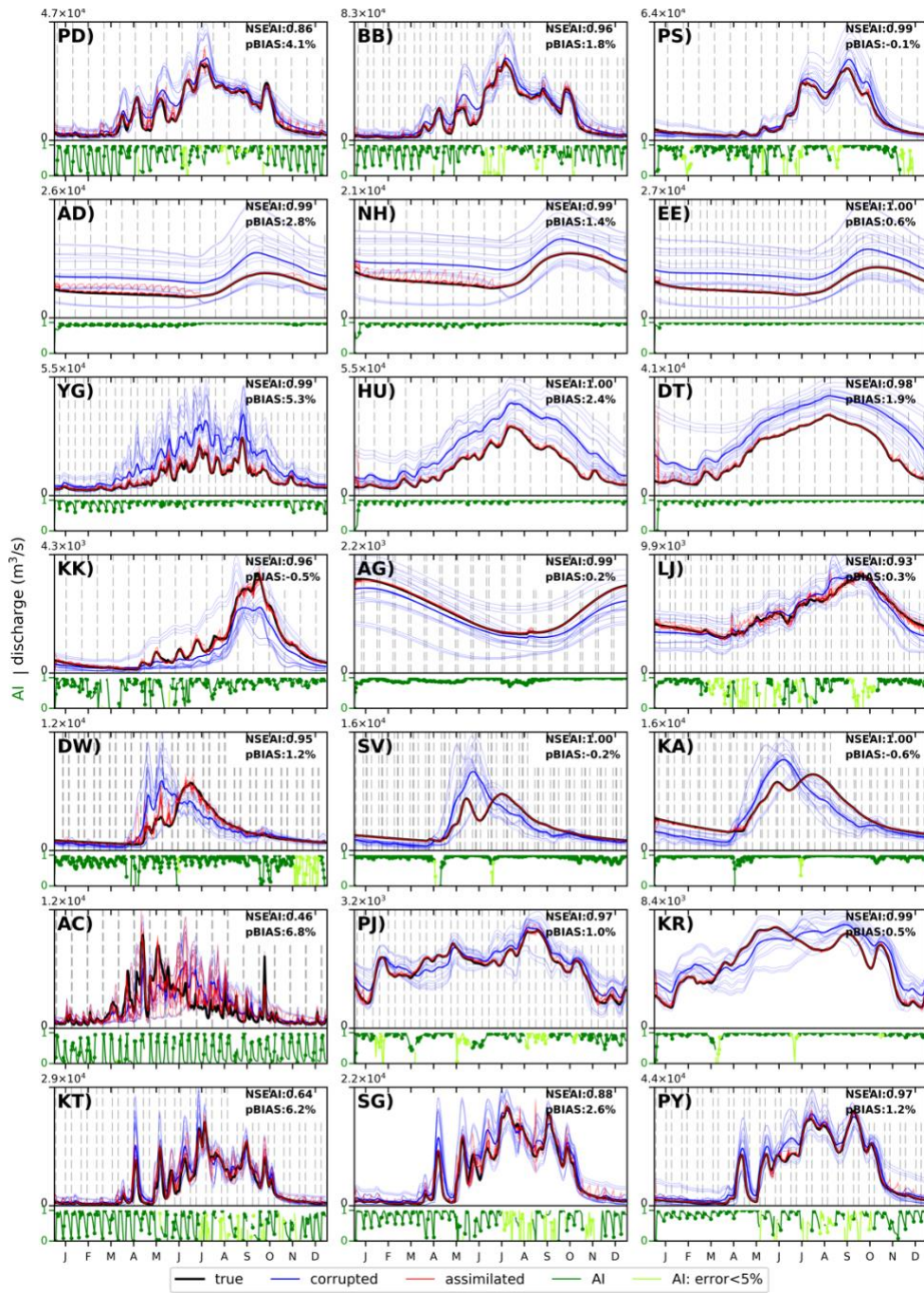


Figure 7. (continued)

574 Small upstream river reaches located at high latitudes had high NSEAI values, whereas
 575 similar river sections at low latitudes had lower NSEAI values. River reaches flowing toward
 576 Hudson Bay in North America had high NSEAI values (> 0.7), whereas upstream river reaches in
 577 high-mountain Asia had low NESAI values (< 0.4; Figure 8). A similar trend was observed in the
 578 hydrographs of most upstream locations of the Indus (Attock [AC]) and Irrawaddy (Katha [KT])

Table 2 : Summary of Figure 7, including river name, station name, location of station, upstream catchment area, number of accumulated overpasses per SWOT cycle, NSEAI, as well as pBias for assimilated and corrupted simulations.

	River	Station	Longitude [°]	Latitude [°]	Catchment Area [km ²]	Accumulated Overpasses	NSEAI	pBias [%] (assimilated)	pBias [%] (corrupted)
SP)	Amazon	Sao Paulo de Olivenca	-68.73	-3.41	1009573	525	0.99	-0.11	-4.26
MP)		Manacapuru	-60.14	-3.33	2204488	1172	1.00	-0.02	-5.06
OP)		Obidos - Porto	-55.50	-1.94	4672153	2490	1.00	0.00	-4.14
KD)	Congo	Kindu	25.87	-2.74	785477	419	0.92	-0.36	8.51
PV)		Ponthierville	25.50	-0.29	932105	496	0.85	0.64	3.75
KH)		Kinshasa	15.25	-4.32	3606257	1972	0.74	0.95	0.47
NK)	Mekong	Nong Khai	102.83	17.95	304814	185	0.92	2.05	16.45
ST)		Stung Treng	105.93	13.50	637963	43	0.90	-0.64	6.28
PK)		Prek Kdam	104.83	11.75	87708	43	0.97	1.67	3.97
KO)	Ob	Kamen'na Obi	81.33	53.87	212392	182	0.99	1.51	9.02
BY)		Belogor'ye	68.50	61.08	2227911	2075	1.00	0.84	31.53
SH)		Salekhard	66.58	66.64	2490615	2439	1.00	-0.16	24.64
SY)	Lena	Solyanka	120.75	60.48	774718	741	0.99	0.00	6.21
ZN)		Zmeinovo	108.56	57.96	139284	127	0.94	3.11	43.46
SB)		Stolb	126.75	72.42	2451204	3089	1.00	-0.40	3.80
AM)	Mississippi	Aitkin, MN	-93.76	46.56	14914	16	0.82	32.64	93.98
AL)		Alton, ill.	-90.34	38.94	443250	270	0.97	9.03	86.23
VM)		Vicksburg, MS	-90.97	32.25	2932631	2048	0.95	1.23	23.18
RG)	Volga	Rybinskaya Ges	39.00	58.04	152867	170	0.99	2.03	-0.81
NC)		Naberezhnyye Chelny	52.25	55.70	369824	0	0.99	3.07	32.84
VP)		Volgograd Power Plant	44.61	48.75	1364059	1315	0.99	1.90	30.96
PD)	Ganges-Brahmaputra	Pandu	91.33	26.10	412713	251	0.86	4.13	18.10
BB)		Bahadurabad	89.59	24.92	512475	312	0.96	1.84	17.46
PS)		Paksey	89.30	23.92	941267	558	0.99	-0.13	9.47
AD)	Nile	Aswan dam	32.90	24.12	2911499	1569	0.99	2.81	52.55
NH)		Nag Hammadi	32.13	26.20	2990389	1615	0.99	1.39	34.97
EE)		El Ekhsase	31.27	29.75	3032569	1642	1.00	0.56	46.78
YG)	Yangtze	Yichang	111.32	30.66	976284	5	0.99	5.31	82.21
HU)		Hankou	114.36	30.65	1441953	93	1.00	2.44	69.23
DT)		Datong	117.74	31.03	1677326	1012	0.98	1.91	50.56
KK)	Niger	Koulikoro	-7.50	12.94	118079	65	0.96	-0.51	-24.22
AG)		Ansongo	0.50	15.53	489888	271	0.99	0.22	-11.12
LJ)		Lokoja	6.75	7.67	1990463	1078	0.93	0.27	-1.39
DW)	Yukon	Dawson	-139.50	64.15	265258	292	0.95	1.24	1.97
SV)		Stevens Village Ak	-149.79	65.88	501116	762	1.00	-0.21	-1.55
KA)		Kaltag, alas.	-158.65	64.20	756273	1177	1.00	-0.55	-11.11
AC)	Indus	Attock	72.24	33.90	199682	132	0.46	6.77	9.90
PJ)		Panjnad	71.00	29.33	278545	169	0.97	0.99	6.31
KR)		Kotri	68.33	25.25	830667	515	0.99	0.48	10.08
KT)	Irrawaddy	Katha	96.27	23.96	84522	51	0.64	6.17	14.54
SG)		Sagaing	95.99	21.87	124739	22	0.88	2.60	15.03
PY)		Pyay	95.16	18.70	360734	206	0.97	1.21	13.61

579 rivers (Figure 7). These incremental changes in the NSEAI values of small river reaches occur
580 because of the frequent SWOT observations recorded at high latitudes. At low latitudes,
581 observation frequencies are much lower. Within the 21-day orbital cycle of the SWOT satellite
582 (Figure 3b), there will be more than four observations at high latitudes ($> 50^\circ$ N), compared to
583 only one or two observations at low latitudes. Note that assimilation frequencies are high because
584 we used an adaptive empirical local patch in the LETKF data assimilation framework. The number
585 of assimilations in the 21-day orbital cycle was more than 10 days at $> 50^\circ$ N and less than 10 days
586 at $< 30^\circ$ N. However, large rivers, such as the downstream reaches of the Amazon River can be
587 assimilated almost every day. Therefore, the assimilation efficiency of small river reaches depends
588 on assimilation frequency.

589 Due to the high frequency of SWOT observations, rivers located at high latitudes had high
590 NSEAI values, even at upstream locations. Figure 9 shows the relationship between NSEAI values
591 and upstream drainage area, taking latitude into account. The black dotted line in Figure 9a shows
592 the relationship between NSEAI values and drainage area, whereas the gray curve indicates the $1-\sigma$
593 range. At low latitudes, upstream reaches and small rivers had small NSEAI values (Figure 9b)

619 be seen with the size of upstream drainage area where NSEAI was increasing with the upstream
 620 drainage area. According to the Figure 10a, it can be expected NESAI will be > 0.8 in the locations
 621 where the accumulated overpasses per SWOT cycle > 100 . NSEAI become almost 1.0 in the river
 622 pixels with accumulated overpasses per SWOT cycle > 565 . However, a slight deviation from high
 623 NSEAI was observed in the river reaches where accumulated overpasses are between 1901-2000.

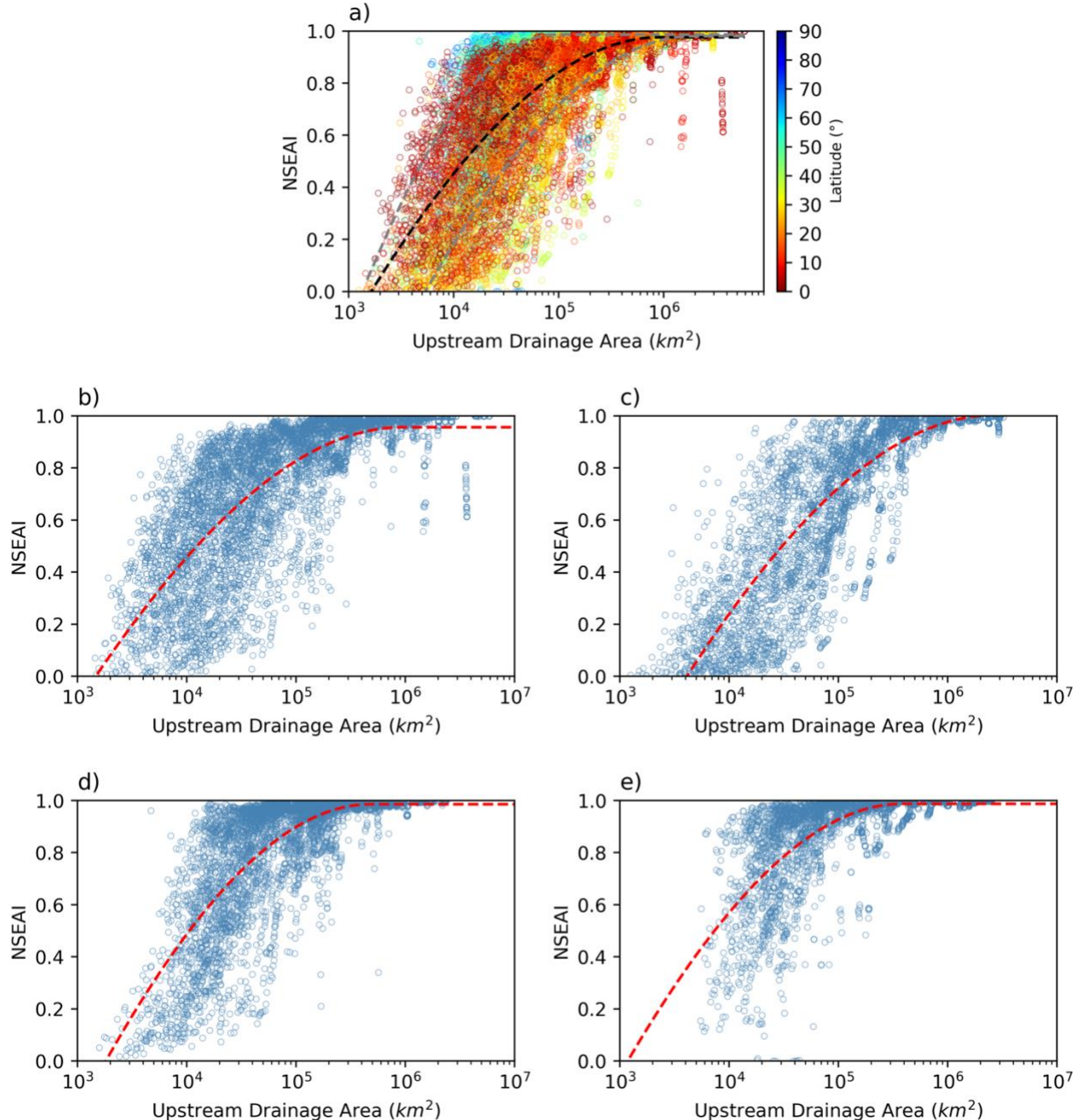


Figure 9 : Relationship between the upstream drainage area and NSEAI: a) for whole globe; b)-e) are for latitudes between 0° - 20° , 21° - 40° , 41° - 60° , 61° - 80° , respectively. The dashed-black line in panel a) and dashed-red lines in panels b)-e) presents the fitted curves for the mean values. The dashed-grey line shows the $1-\sigma$ range for the fitted mean curve. Pixels with annual mean discharge > 100 m^3/s are shown. The colors in panel a) show the latitude of each pixel.

624 Those NSEAI deviation are due to the low NSEAI values of the downstream reaches of Congo
 625 river because the corrupted simulation efficiency in the downstream reaches of Congo river was
 626 high ($NSE > 0.8$). Hence, higher assimilation efficiency is expected in places where the number of
 627 accumulated overpasses per SWOT cycle higher assimilation efficiency is expected in places
 628 where the accumulated overpasses are higher in the perfect model scenario.

629 The assimilation frequency depends on the size of the adaptive empirical local patch. The
 630 assimilation frequency was defined as the number of assimilations per SWOT cycle which
 631 represents the local correction of each river pixel where higher assimilation frequency tends to
 632 produce high NSEAI values (Figure 10b). A global map of assimilation frequency is presented in
 633 supplementary information section (Figure S7). Empirical local patches in the upstream reaches is
 634 smaller than that of the downstream reaches (Revel et al., 2019). As explained above small
 635 upstream river reaches have low NSEAI compared to downstream. The NSEAI values are > 0.8 in
 636 the river reaches where the assimilation frequency per SWOT cycle > 11 . Large variation in the
 637 NSEAI in 8-11 assimilation frequency band can be due to the variation of accumulated overpasses
 638 per SWOT cycle. Hence, both accumulated overpasses and assimilation frequency contributes to
 639 the assimilation efficiency of our assimilation framework.

640 The contribution of the accumulated overpasses and the assimilation frequency can be
 641 illustrated by the Figure 10c. Mean NSEAI at each assimilation frequency and accumulated
 642 overpass is shown as 2-dimensional map where colors indicate the mean NSEAI and contours

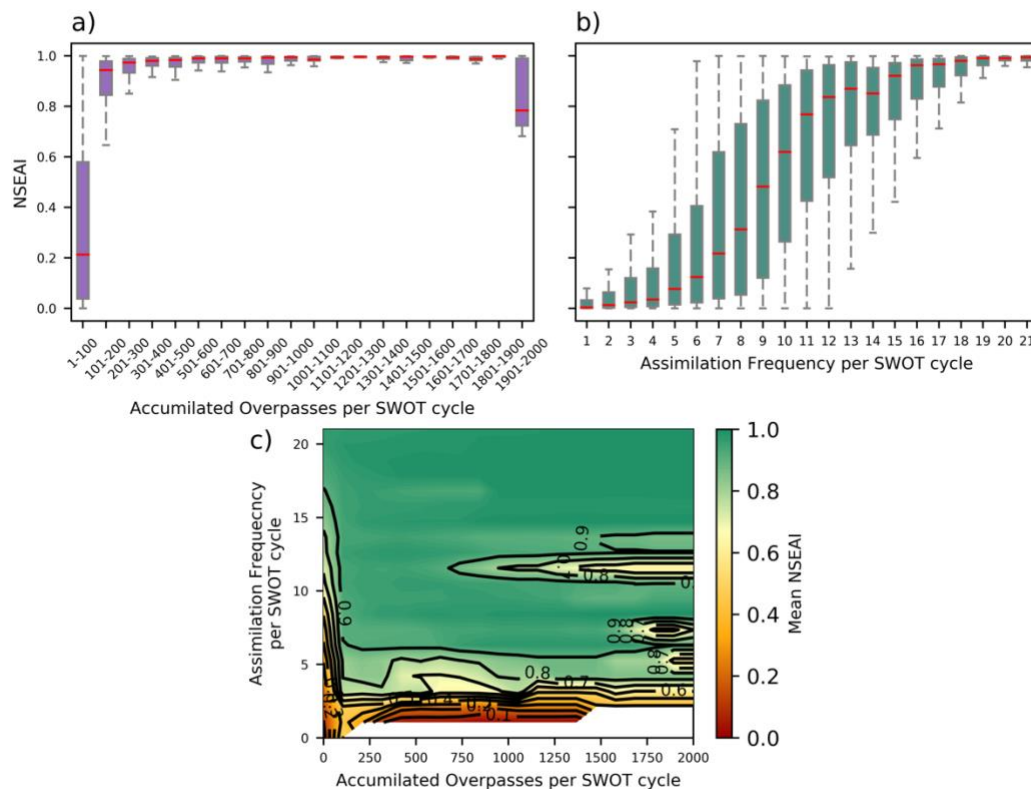


Figure 10: Boxplot of NSEAI with a) accumulated overpasses and b) assimilation frequency per SWOT cycle. c) Mean NSEAI variation with accumulated overpasses and assimilation frequency. Panel a is between 1-2000 accumulated overpasses and the data are presented in 100-overpass category intervals.

643 from 0.0~1.0 is plotted at 0.1 interval (black lines in Figure 10c). The river reaches with higher
 644 assimilation frequency and accumulated overpasses were shown higher NSEAI values (>0.9).
 645 Very high assimilation efficiency can be expected in the places where the accumulated overpasses
 646 > 100 and assimilation frequency > 7 . Therefore, the assimilation efficacy can be explained by the
 647 combination of the accumulated overpasses per SWOT cycle (measure of upstream inflow
 648 correction) and the assimilation frequency (measure of local correction).

649 Continental-scale rivers show high KGE values after synthetic SWOT observations have
 650 been assimilated. Figure 11 shows a boxplot of KGE values for assimilated discharge in
 651 continental -scale rivers. Here, we show the five rivers with the largest catchment areas for each
 652 latitude band. All the rivers shown in Figure 11 have median KGE values > 0.6 . KGE values
 653 provide diagnostic insight into the performance of our assimilation framework in river discharge
 654 estimates. The KGE value combines correlation, relative bias, and variability to reproduce
 655 temporal dynamics while preserving flow durations. The median KGE values of large low-latitude
 656 rivers were high (KGE > 0.9). The Yangtze River had the lowest KGE value among the 15 rivers
 657 shown in Figure 11 due to low KGE values in the small tributaries south of the river. However,
 658 almost all global rivers showed improved KGE values in assimilated compared to corrupted
 659 simulations (Text S6, Fig. S3). Therefore, the assimilated discharge estimates represented the
 660 hydrodynamics of the rivers accurately, reaching KGE values of > 0.9 for continental-scale rivers.

661 4.2 Imperfect model experiment

662 Here, we describe the results of the imperfect model experiment. Model error was
 663 represented using a spatially distributed Manning's coefficient in the true simulation, whereas a
 664 global constant Manning's coefficient of 0.03 was used in the assimilated and corrupted

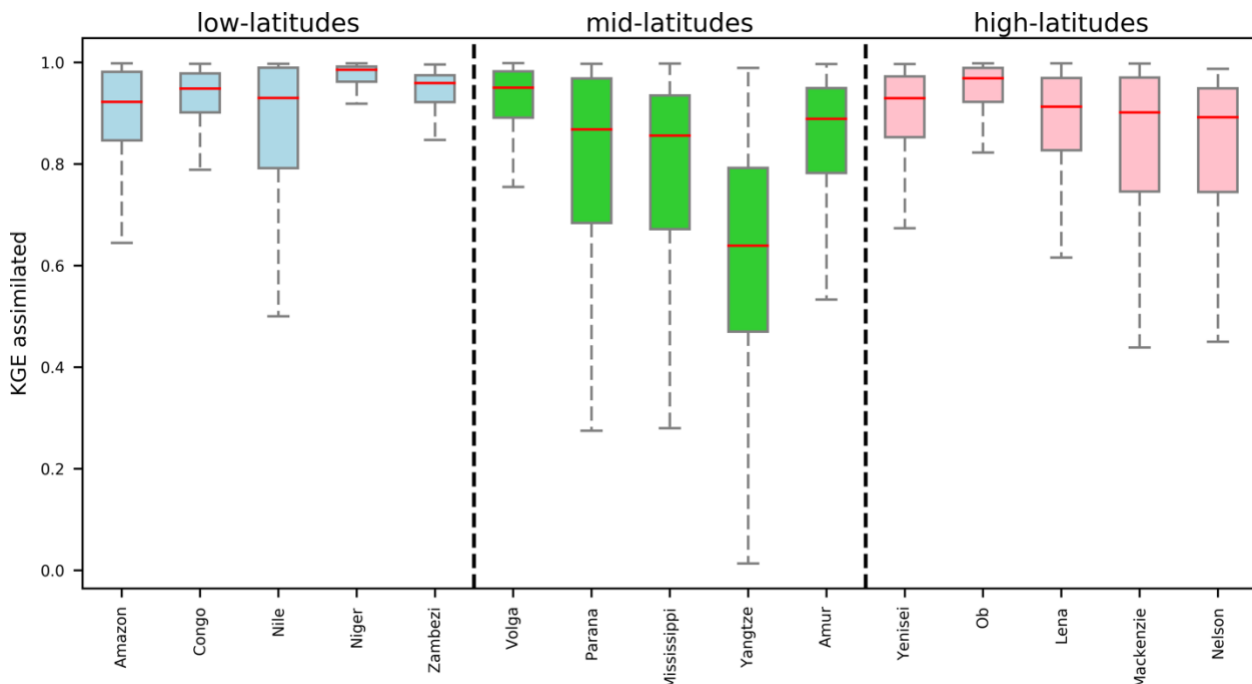


Figure 11: Kling-Gupta efficiency (KGE) of assimilated discharge in the perfect model for continental-scale rivers at low-latitudes (light blue), mid-latitudes (light green), and high-latitudes (pink). River pixels with mean river discharge > 100 m³/s were used to create the boxplot.

665 simulations. Figure 12 shows hydrographs from 42 locations representing upstream, midstream,
666 and downstream locations in 14 rivers. Figure 12 shows a global map of NSEAI values with
667 annotated locations corresponding to those shown in Figure 7. Table 3 summarizes the assimilation
668 efficiency diagnostics and the Manning's coefficient values used in the true simulation for the
669 locations shown in Figure 12. The assimilation efficiency was improved using our data assimilation
670 framework even when the model was imperfect. Most of the hydrographs shown in Figure 12 have
671 high NSEAI values (> 0.7), except for those representing Sao Paulo de Olivenca (SP), Ponthierville
672 (PV), KH, Paksey (PS), Ansongo (AG), AC, KT, and Sagaing (SG). Differences in peak flow
673 timing between the true and corrupted simulations are observed in the hydrographs (Figure 12).
674 These were due to differences in the Manning's coefficients used in each simulation. Wave
675 propagation in the true and assimilated/corrupted simulations differed due to differences in the
676 Manning's coefficient values used and in the local inertial equation (Bates et al., 2010; Yamazaki
677 et al., 2011). By assimilating SWOT observations, we were able to improve peak discharge timing
678 estimates (Figure 12). However, estimates of peak discharge differed slightly from the true values
679 due to changes in the local stage discharge relationship which, in turn, were caused by differences
680 in the Manning's coefficient values used for the true and was not corrected instantaneously. In
681 conclusion, NSEAI values were high at most locations shown corrupted/assimilated simulations.
682 It should be noted that we assimilated WSE, river discharge in Figure 12, even in the imperfect
683 model.

684 Although WSE was incorporated into the CaMa-Flood hydrodynamic model, the
685 magnitude of river discharge differed between assimilated and true simulations. At the Obidos-
686 Porto (OP) location, peak flow was underestimated in the assimilated simulation, whereas low
687 flow estimates were more accurate (Manning's coefficient = 0.0295, Table 3). Peak discharge was
688 also underestimated for the Salekhard (SH), Solyanka (SY), Stolb (SB), Alton, ill (AL), Vicksburg,
689 MS (VM), PS, Aswan Dam (AD), Nag Hammadi (NH), El Ekhsase (EE), KA and Kotri (KR)
690 locations because the values used for Manning's coefficient in the true simulations (Table 3) were
691 lower than those used in the assimilated/corrupted simulations. Peak discharge was slightly
692 overestimated at the Rybinskaya Ges (RG), AG, and Panjnad (PJ) locations (Manning's coefficient
693 > 0.030 in the true simulation). Nonetheless, discrepancies in peak river discharge may not affect
694 NSEAI values if Manning's coefficient values vary significantly (e.g., at the SH, SY, AL, PS, NH,
695 and EE locations). This is because the seasonal hydrodynamics of river flow play important roles
696 in determining NSEAI. Therefore, overestimation and underestimation of peak discharge in the
697 assimilated simulations highlights a major limitation of our assimilation framework, which must
698 be addressed.

699 Major discrepancies were observed in NSEAI values at some locations (e.g., SP, PV, KH,
700 SB, PS, AG, AC, KT, and SG) where corrupted simulations were coincidentally similar to true
701 simulations. The NSEAI value at the AG location on the Niger River was extremely low (0.04)
702 compared to other continental-scale rivers and had a Manning's coefficient of 0.0325 in the true
703 simulation. This decrease in assimilation efficiency occurred because the corrupted river discharge
704 was similar to the true discharge value. The NSE values for the corresponding corrupted and
705 assimilated simulations were very similar (0.93). Therefore, improvements due to the assimilation
706 of SWOT observations were not apparent. In addition, NSEAI values do not reflect assimilation
707 efficiency if the NSE values in the corrupted simulations are close to 1.0 because this is the
708 maximum value. The corrupted simulations were very similar to the true simulations and had NSE

709 values > 0.9 at the SP, PV, KH, PS, KT, and SG locations. In contrast, there were low NSEAI

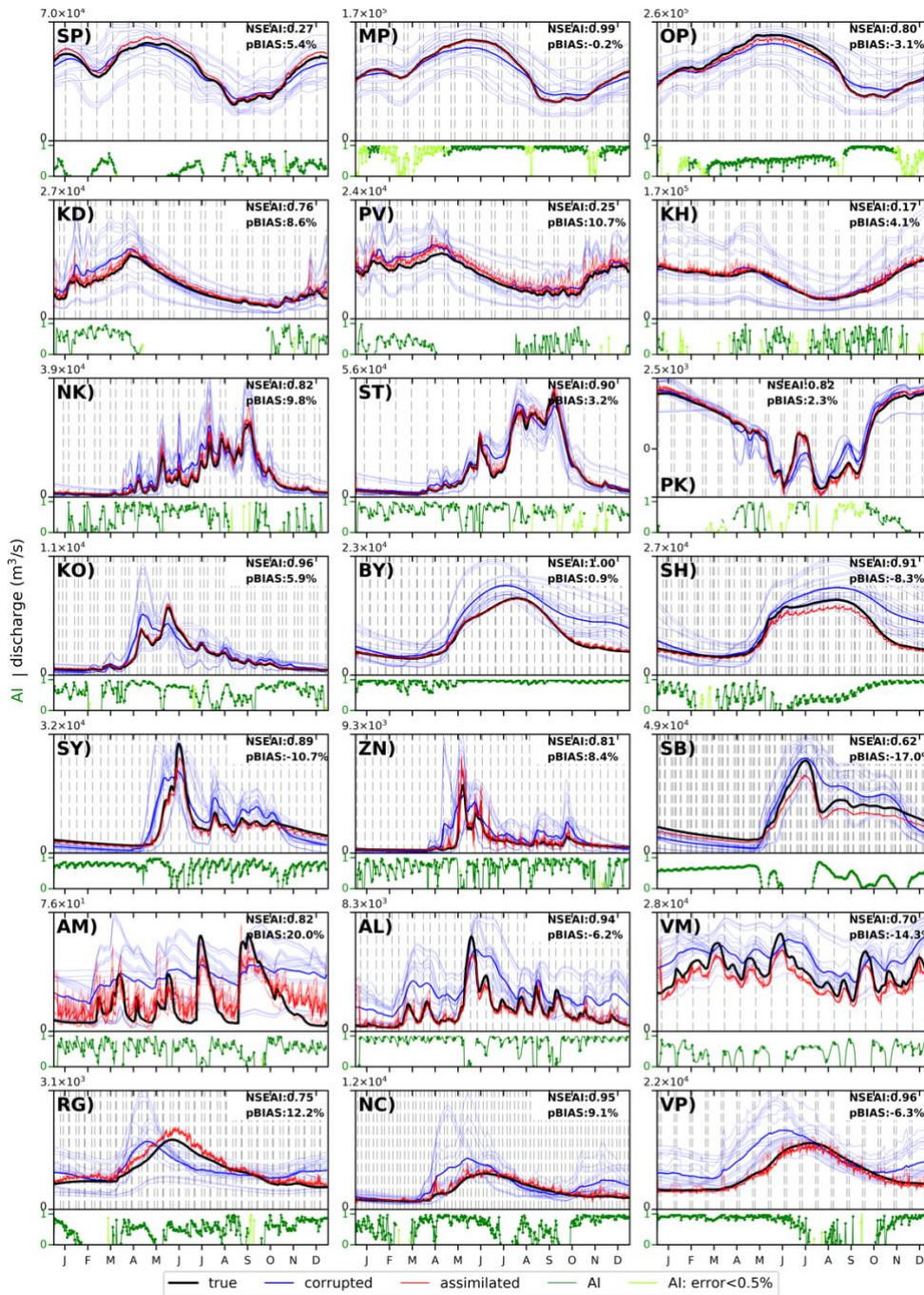


Figure 12 : Simulated discharge for the imperfect model experiment on a global scale. The locations are summarized in Table 3. River discharges of true, assimilated, and corrupted simulations are shown by black, red, and light blue lines, respectively. Dark-blue line represent the ensemble mean of corrupted simulation. The dashed-grey lines indicate the times of direct SWOT observations. The AI (green line in lower panel) is shown for days when the error between the true and corrupted discharges was $> 5\%$. Light green line indicates the AI when error was $< 5\%$. Green dots represent the times of data assimilation. The colors and key are identical to those shown for Figure 5a-c.

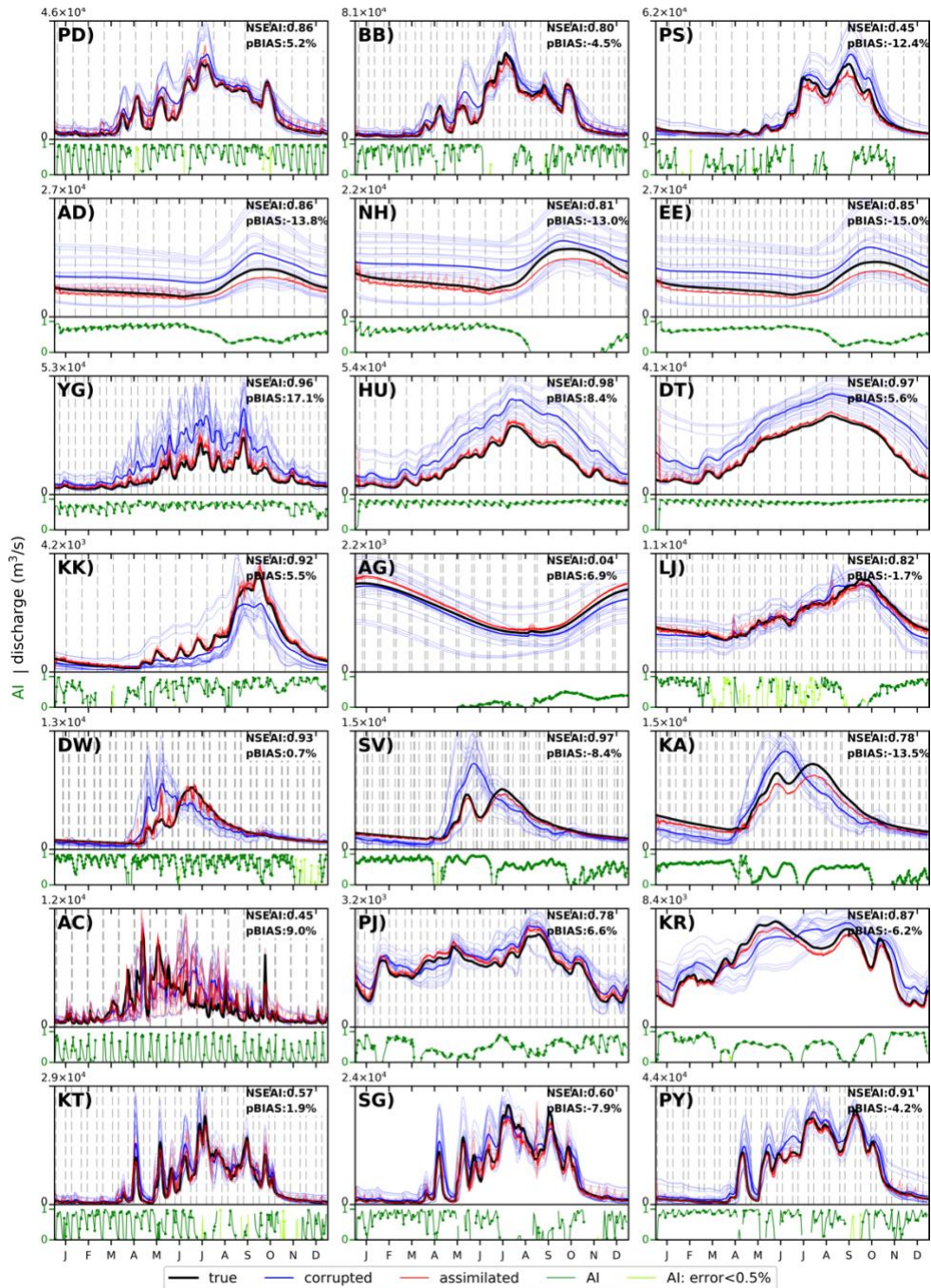


Figure 12. (continue)

710 values at the SB (0.62) and AC (0.45) locations. Assimilated discharge was underestimated at the
 711 SB location on the Lena River due the difference in the Manning's coefficient in true simulation
 712 (0.025). On the other hand, few observations were available for the AC location, situated in the
 713 upstream reaches of the Indus River (Manning's coefficient in true simulation is almost 0.03).
 714 However, all locations shown in Figure 12 had positive NSEAI values, indicating that assimilated
 715 discharge estimates were more similar to the true simulation than the corrupted simulation.
 716 Therefore, low assimilation scores in large rivers were due to corrupted and true discharge values
 717 being coincidentally similar.

Table 3: Summary of Figure 12, including station name; Manning's coefficient for true simulation, NSEAI, as well as pBias for assimilated and corrupted simulations.

	Station	Manning's Coefficient [$s/m^{2/3}$] (true simulation)	NSEAI	pBias[%] (assimilated)	pBias [%] (corrupted)
SP)	Sao Paulo de Olivenca	0.0328	0.27	5.45	-1.53
MP)	Manacapuru	0.0276	0.99	-0.24	-3.23
OP)	Obidos - Porto	0.0295	0.80	-3.10	-3.78
KD)	Kindu	0.0322	0.76	8.57	10.48
PV)	Ponthierville	0.0340	0.25	10.71	10.12
KH)	Kinshasa	0.0281	0.17	4.06	2.26
NK)	Nong Khai	0.0324	0.82	9.80	18.58
ST)	Stung Treng	0.0275	0.90	3.23	8.14
PK)	Prek Kdam	0.0326	0.82	2.31	8.50
KO)	Kamen'na Obi	0.0292	0.96	5.88	10.74
BY)	Belogor'ye	0.0273	1.00	0.87	33.01
SH)	Salekhard	0.0250	0.91	-8.32	26.88
SY)	Solyanka	0.0250	0.89	-10.68	7.80
ZN)	Zmeinovo	0.0292	0.81	8.36	46.07
SB)	Stolb	0.0250	0.62	-17.00	4.23
AM)	Aitkin, MN	0.0343	0.00	19.99	90.09
AL)	Alton, ill.	0.0250	0.94	-6.21	89.38
VM)	Vicksburg, MS	0.0250	0.70	-14.29	24.55
RG)	Rybinskaya Ges	0.0334	0.75	12.24	4.99
NC)	Naberezhnyye Chelny	0.0318	0.95	9.12	36.04
VP)	Volgograd Power Plant	0.0326	0.96	-6.29	34.19
PD)	Pandu	0.0313	0.86	5.23	20.83
BB)	Bahadurabad	0.0262	0.80	-4.46	16.24
PS)	Paksey	0.0250	0.45	-12.43	10.47
AD)	Aswan dam	0.0250	0.86	-13.80	42.82
NH)	Nag Hammadi	0.0259	0.81	-12.98	31.19
EE)	El Ekhsase	0.0256	0.85	-14.97	42.32
YG)	Yichang	0.0329	0.96	17.08	85.29
HU)	Hankou	0.0296	0.98	8.35	71.90
DT)	Datong	0.0318	0.97	5.56	53.06
KK)	Koulikoro	0.0326	0.92	5.52	-22.58
AG)	Ansongo	0.0325	0.04	6.92	-6.69
LJ)	Lokoja	0.0284	0.82	-1.71	-3.38
DW)	Dawson	0.0285	0.93	0.74	4.03
SV)	Stevens Village Ak	0.0282	0.97	-8.40	0.36
KA)	Kaitag, alas.	0.0261	0.78	-13.51	-11.50
AC)	Attock	0.0299	0.45	8.95	11.81
PJ)	Panjnad	0.0323	0.78	6.60	11.15
KR)	Kotri	0.0290	0.87	-6.17	8.72
KT)	Katha	0.0268	0.57	1.91	14.74
SG)	Sagaing	0.0251	0.60	-7.95	12.39
PY)	Pyay	0.0315	0.91	-4.19	15.86

718 Figure 13 shows global map of NSEAI values for the imperfect model experiment. In
719 general, the level of variation among NSEAI values in the perfect and imperfect model
720 experiments was similar. Continental-scale rivers showed high NSEAI values (> 0.8) in
721 downstream reaches at low latitudes and all river reaches at high latitudes. Small upstream river
722 reaches at high latitudes showed higher NSEAI values (> 0.8) than those at low latitudes (NSEAI
723 < 0.7 ; e.g., upstream reaches and tributaries of the Amazon and Congo rivers). However, almost
724 all of these rivers had positive NSEAI values. Therefore, discharge estimates in all river reaches
725 were improved by implementing our data assimilation framework. Consequently, global analysis
726 (Figure 12) showed that our assimilation framework improved the accuracy of river discharge

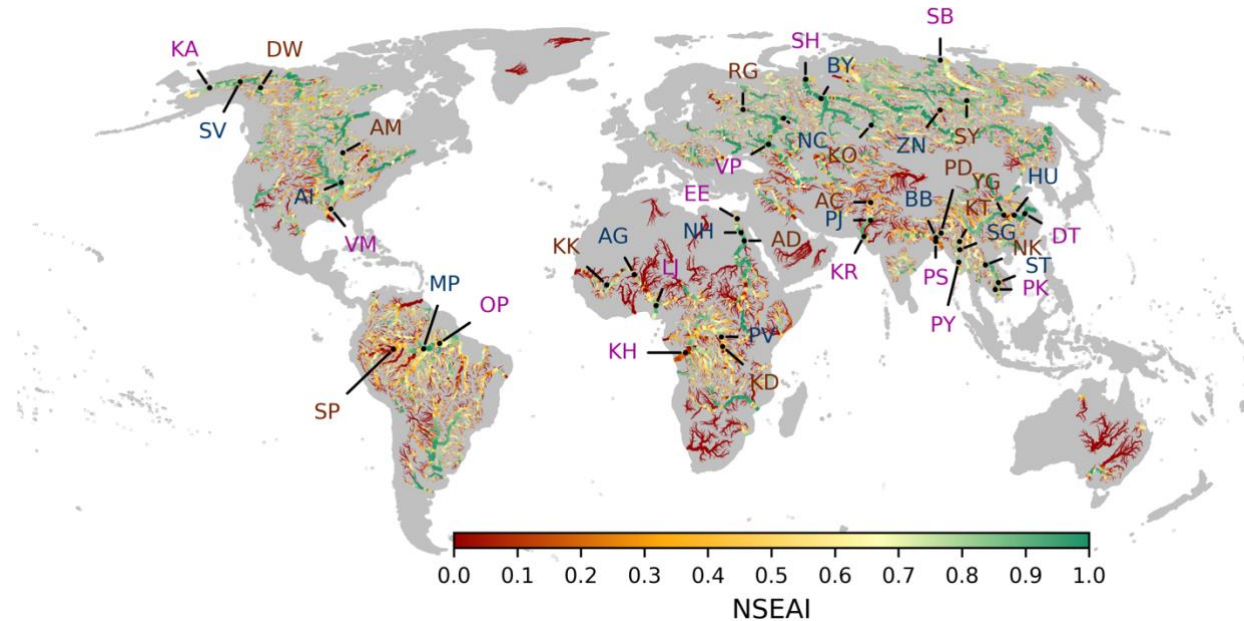


Figure 13: Global NSEAI map for the imperfect model experiment. The annotations correspond to the panels shown in Figure 12. Upstream, midstream, and downstream annotations are shown in brown, blue, and purple, respectively.

727 estimates in continental-scale rivers. Figure 13 shows that NSEAI values were generally lower in
 728 the imperfect model experiment than in the perfect model experiment. The NSEAI was designed
 729 to evaluate the effectiveness of data assimilation in a perfect model with unrealistic input runoff
 730 forcing. However, here we used the NSEAI to assess the assimilation efficiency of the imperfect
 731 model experiment. The midstream reaches of large rivers exhibited higher NSEAI values than
 732 downstream and upstream reaches (Table 3). A Manning's coefficient of 0.030 was used for
 733 corrupted/assimilated simulations, whereas different Manning's coefficients were used in the
 734 imperfect model experiment for true simulations, depending on river width. Discrepancies in
 735 NSEAI values corresponded to the magnitude of model error, as discussed below. However,
 736 assimilation efficiencies for the downstream reaches of large rivers exhibited greater discrepancies
 737 in the imperfect than in the perfect model experiment (e.g., the Congo, Ob, and Lena rivers;
 738 Figure 12).

739 Assimilation efficiencies were correlated with the magnitude of model error. Figure 14
 740 shows a scatter plot of NSEAI values with upstream drainage areas (Figure 14a) and the total
 741 number of accumulated overpasses per SWOT cycle (Figure 14b) compared to the magnitude of
 742 model error in the imperfect model experiment. Here, we define the magnitude of model error as
 743 the absolute difference in the Manning's coefficient for the true and corrupted/assimilated
 744 simulations. In Figure 14, the magnitude of model error is separated into five categories, based on
 745 absolute Manning's coefficient errors. Mean curves for each category are shown in Figure 14a and
 746 b. River reaches with large upstream drainage areas had low NSEAI values when the model error
 747 was large, and vice versa. However, in small river reaches (upstream drainage area $< 1 \times 10^5$ km²),
 748 variations in NSEAI values were not reflected by the magnitude of model error. As in the perfect
 749 model experiment (Figure 10a), NSEAI values reached a maximum level after 1000 accumulated
 750 overpasses in each model. The fitted curves show that the assimilation score was high when the

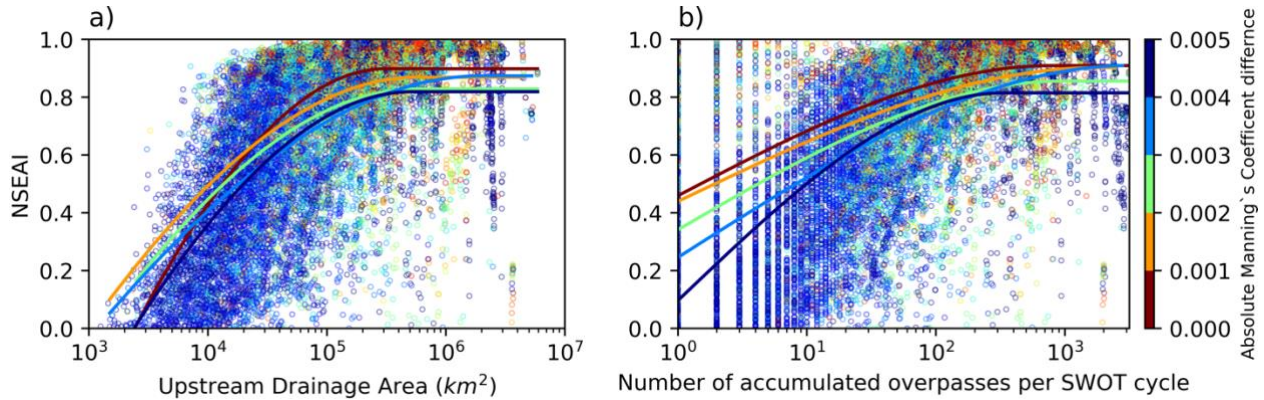


Figure 14: Scatter plot comparing NSEAI with a) upstream drainage area and b) accumulated overpasses per SWOT cycle based on the Manning's coefficient error for the imperfect model experiment.

751 Manning's coefficient error was low (shown in red in Figure 14), and when the model error was
 752 high the assimilation efficiency was low (shown in violet in Figure 14). However, it is difficult to
 753 discern a clear relationship from Figure 14. However, mean variation in NSEAI values is inversely
 754 related to assimilation efficiency and model error. Therefore, the magnitude of model error has an
 755 important impact on assimilation efficiency.

756 Figure 15 is a boxplot showing KGE values for 15 continental-scale rivers at low, mid, and
 757 high latitudes. All of these continental-scale rivers had median KGE values of > 0.6 , which
 758 corresponds to good model efficiency. Large rivers at low latitudes showed good assimilation,
 759 with median KGE values > 0.8 . Similarly, rivers at high latitudes also had high median KGE values
 760 (> 0.8). Rivers at mid latitudes had slightly lower median KGE values. Although the Yangtze River
 761 had the lowest median KGE value (~ 0.6), the main stem of the river was well-characterized by our
 762 framework (Figure S4). Small tributaries in the south of Yangtze River showed low KGE values
 763 (~ 0.5) which caused reduction of median KGE. River discharge estimates in most of the
 764 continental-scale rivers were better in the assimilated simulation than in the corrupted simulation
 765 (Text S6 and Figure S4). Therefore, river discharge estimates for continental-scale rivers were
 766 generally good.

767 4.3 Perfect model vs. imperfect model experiments

768 In the perfect model experiment, we assumed that model error was avoidable, whereas in
 769 the imperfect model experiment, we assumed that model error was included in Manning's
 770 coefficient. Our data assimilation framework produced good results in both experiments. In
 771 general, the perfect model experiment had higher assimilation scores (i.e., NSEAI values) than the
 772 imperfect model experiment. Figure 16 shows a boxplot of KGE values for the assimilated
 773 simulation with different numbers of accumulated overpasses per SWOT cycle for the perfect
 774 (Figure 16a) and imperfect (Figure 16b) model experiments. KGE values offer diagnostic insight
 775 into the performance of our assimilation framework in river discharge estimates. The KGE value
 776 combines correlation, relative bias, and variability to reproduce temporal dynamics while
 777 preserving flow durations. The graph in Figure 16 shows the total number of 1–600 overpasses on
 778 the horizontal axis in 20-overpass category intervals. In both experiments, the KGE values were $>$
 779 0.6 in almost all the river reaches in the assimilated simulation. There were large variations in both
 780 experiments when the total number of accumulated overpasses per SWOT cycle was < 250 .
 781 However, in the perfect model experiment, median KEG values were ≥ 0.95 in river reaches with

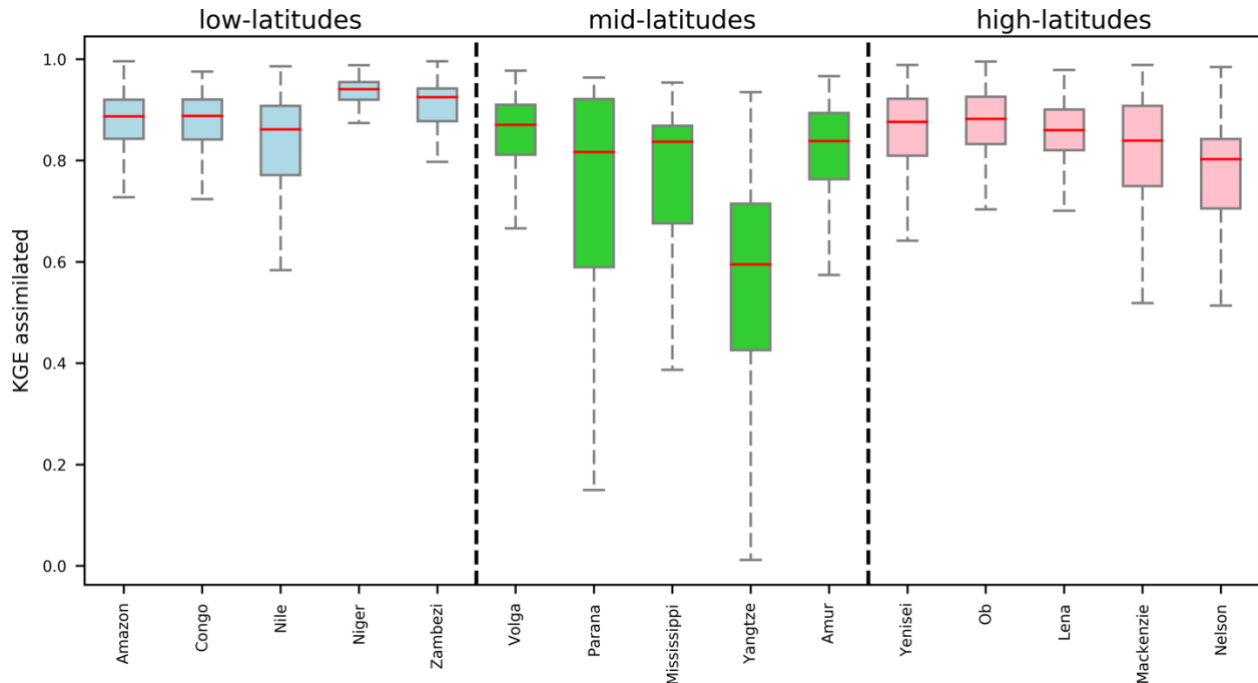


Figure 15: KGE of assimilated discharge in the imperfect model experiment for continental-scale rivers at low-latitudes (light blue), mid-latitudes (light green), and high-latitudes (pink). River pixels with a mean river discharge $> 100 \text{ m}^3/\text{s}$ were used to create the boxplot.

782 > 270 accumulated overpasses per SWOT cycle. The KGE values varied little in places where
 783 there were > 270 accumulated overpasses. In the imperfect model experiment, variation in KGE
 784 values was lower when there were > 270 overpasses per SWOT cycle. Therefore, minimizing
 785 model errors (i.e., in Manning's coefficient) is important for accurately assimilating SWOT
 786 observations.

787 5. Summary and Discussion

788 In this study, we developed a framework for global data assimilation using physically-
 789 based empirical localization parameters and the LETKF algorithm. We generated synthetic SWOT
 790 observations using simulated WSE measurements from the CaMa-Flood global hydrodynamic
 791 model, satellite orbit information, and expected observation errors. We evaluated the effectiveness
 792 of data assimilation on global river discharge estimates using OSSEs. The effectiveness of
 793 assimilation was evaluated using a perfect model in which the hydrodynamic model was error free
 794 and an imperfect model in which model error was included in Manning's coefficient. In the perfect
 795 model experiment, we used similar parameters for the true, corrupted, and assimilated simulations,
 796 whereas different runoff forcing was applied in the true and corrupted/assimilated simulations. In
 797 contrast, different model parameters (e.g., Manning's coefficient values) were used in the true and
 798 corrupted/assimilated simulations, and different runoff forcing was applied in the imperfect model
 799 experiment.

800 The perfect model experiment was performed using different runoff forcing in true and
 801 corrupted/assimilated simulations. River discharge simulations were significantly improved by
 802 data assimilation at most continental-scale river locations, particularly those at high latitudes
 803 ($> 50^\circ$) and in downstream river reaches at low latitudes. Discharge at upstream locations was well-

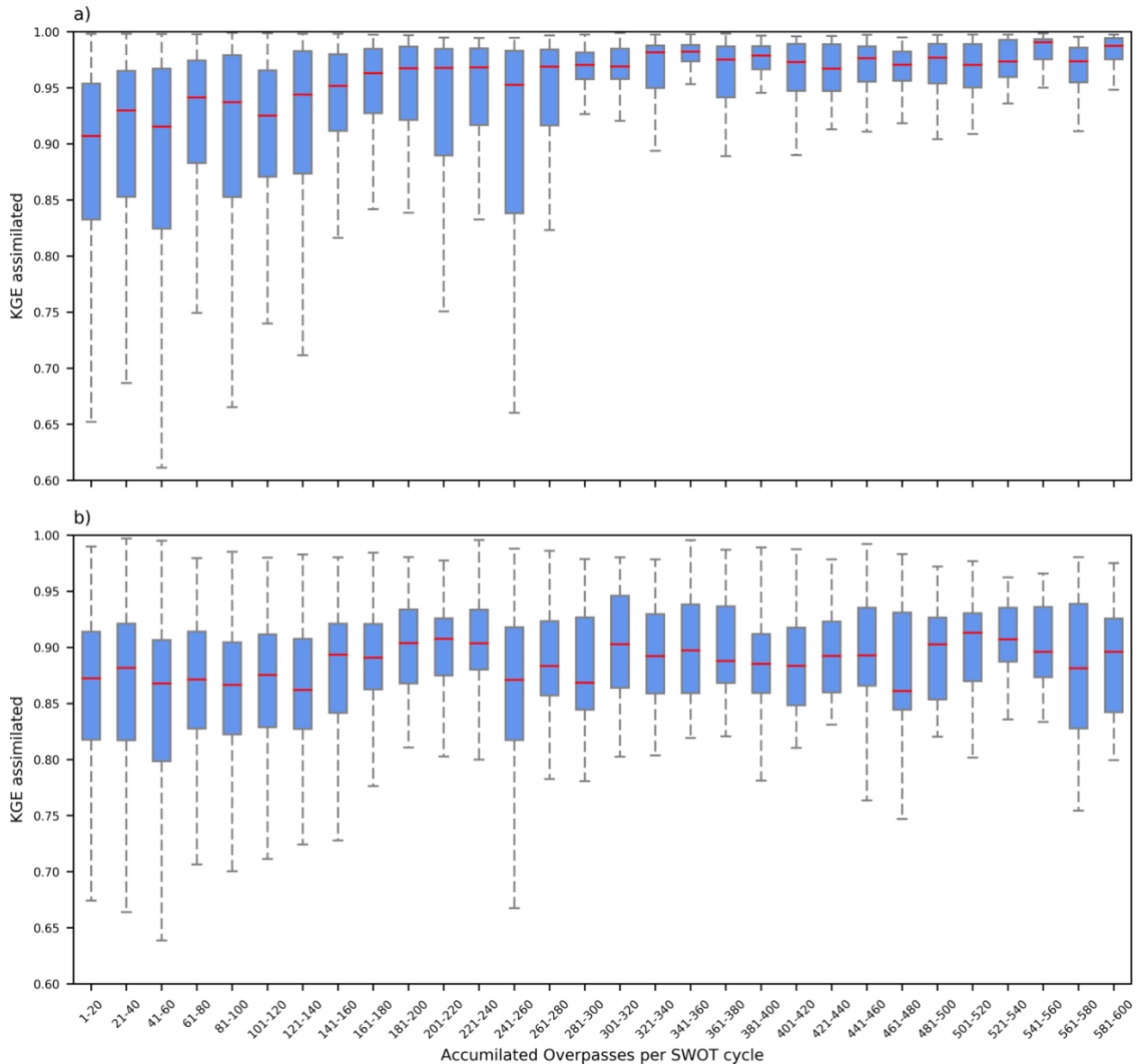


Figure 16: Boxplot of KGE values for assimilated simulation of a) perfect model and b) imperfect model experiments compared with the accumulated overpasses per SWOT cycle. There were between 1-600 accumulated overpasses. The data are presented in 20-overpass category intervals.

804 characterized on days on which local observations are available. However, the assimilation
 805 efficiency decreased on days on which there was no local observations. Nonetheless, at
 806 downstream locations, the assimilation efficiency was consistently high even on days in which
 807 there were no local observations. Rivers located at high latitudes also had high assimilation
 808 efficiencies in most river reaches, including upstream locations. Therefore, river discharge
 809 estimates in continental-scale rivers were improved by assimilating the SWOT observations.

810 The size of the empirical local patch and the number of upstream observations contributed
 811 to the low assimilation efficiency of upstream river reaches (Figure 10). Local patches in upstream
 812 river reaches were smaller than those in downstream river reaches (Revel et al., 2019), which

813 decreased the number of assimilations per SWOT cycle. If the empirical local patch is reduced in
814 size, the water state of an assimilated pixel may not be consistent with that of adjacent pixels,
815 resulting in sudden changes in both WSE measurements and discharge at the target pixel.
816 Moreover, the inflow correction from upstream is low in upstream river reaches. At upstream
817 locations, differences between assimilated and true discharge were due to fewer local and upstream
818 observations (Figure 5a). We used adaptive empirical local patches (Revel *et al.*, 2019) to
819 incorporate information from distant pixels and reduce inconsistencies in WSE measurements after
820 assimilation. However, inconsistent WSE measurements may occur when target pixels are found
821 in upstream river reaches. The coverage of SWOT observations may be improved by interpolating
822 SWOT observations in upstream river reaches (Yoon *et al.*, 2013).

823 The imperfect model experiment, which assumed the presence of errors, implied that river
824 hydrodynamics, such as annual mean flow or flood peak timing, may be evaluated by assimilating
825 SWOT observations even when realistic forcing data and parameters are unavailable.
826 Instantaneous corrections from SWOT observations could not be directly applied to river discharge
827 estimates because we assimilated WSE measurements only. Generally, assimilation efficiency was
828 lower in the imperfect model experiment than in the perfect model experiment. However, global
829 river discharge estimates were improved by incorporating SWOT observations even when model
830 parameter errors and unrealistic runoff forcing were included. In addition, the KGE value for
831 assimilated discharge was > 0.6 in most river reaches. As the model error is strongly associated
832 with data assimilation effectiveness, improving our model is essential for generating more accurate
833 river discharge estimates using SWOT observations and data assimilation. However, some of the
834 downstream reaches of large rivers (e.g., the Congo River) showed decreased assimilation
835 efficiencies because the corrupted discharge was coincidentally similar to the true discharge.

836 Further studies are needed to define the geographical parameters for hydrodynamic
837 modeling using satellite altimetry (Durand *et al.*, 2010; Yoon *et al.*, 2012; Pedonetti *et al.*, 2014;
838 Revel *et al.*, 2018; Emery *et al.*, 2019; Breda *et al.*, 2019). Before implementing a global
839 assimilation framework, topography parameters for river hydrodynamic models must be carefully
840 defined. Increasing the accuracy of global digital elevation models (DEMs) (O'Loughlin *et al.*,
841 2016; Yamazaki *et al.*, 2012, 2017, 2019) is essential because all river hydrodynamic models use
842 DEMs for their baseline topography data. Realistic representations of channel cross-sections (i.e.,
843 width and bathymetric depth) are also needed because these are used to determine flow conveyance
844 capacity. Recently, global-scale river-width datasets have been developed using high-resolution
845 satellite images (Allen & Pavelsky, 2015; Yamazaki *et al.*, 2014). Methods to estimate channel
846 bathymetric depth using SWOT observations have also been proposed (Brêda *et al.*, 2019; Durand
847 *et al.*, 2008; Revel *et al.*, 2018; Yoon *et al.*, 2012). Estimating other hydrodynamic parameters,
848 such as Manning's coefficient, is also essential and may be achieved using SWOT observations
849 (Emery *et al.*, 2019; Pedinotti *et al.*, 2014). River hydrodynamic models will be improved by
850 accurately defining topography parameters. In addition, we must be able to quantify the error
851 associated with data assimilation frameworks that is caused by topographic uncertainties.

852 In this study, we were able to assimilate SWOT observations into a global-scale river
853 model. Furthermore, we demonstrated that this model could be used to estimate river discharge in
854 large river basins. However, to apply this data assimilation framework to real SWOT observations
855 in the near future, further studies on the model physics and ancillary topography data development
856 are needed. In addition, further studies are required to determine how to apply our data assimilation
857 framework to real SWOT observations. The following items must be addressed to ensure our

858 method can be applied to real SWOT observations on a global scale:1. A method is needed to
 859 transform fine (< 100 m) SWOT observations into a form that can be applied to a coarse CaMa-
 860 Flood model grid (~25 km) (discussed in section 3.1), 2. An interpolation method is needed to
 861 smooth WSE measurements at assimilated locations and ensure these are consistent with adjacent
 862 pixels (discussed in section 4.1.1), 3. The accuracy of runoff estimates must be improved
 863 (discussed in section 4.1.2), 4. The accuracy of river models must be improved by precisely
 864 defining geographical parameters such as Manning's coefficient (discussed in section 4.2).

865 6. Acknowledgments

866 Data available from the authors upon request. This research was supported by JSPS Grant-in-Aid
 867 for Scientific Research (16H06291, 18H01540, and 20H02251).
 868

869 7. References

- 870 Allen, G. H., & Pavelsky, T. M. (2015). Patterns of river width and surface area revealed by the
 871 satellite-derived North American River Width data set. *Geophysical Research Letters*,
 872 42(2), 395–402. <https://doi.org/10.1002/2014GL02764>
- 873 Alsdorf, D., Dunne, T., Melack, J., Smith, L., & Hess, L. (2005). Diffusion modeling of
 874 recession flow on central Amazonian floodplains. *Geophysical Research Letters*, 32(21),
 875 1–4. <https://doi.org/10.1029/2005GL024412>
- 876 Andreadis, K. M., Clark, E. A., Lettenmaier, D. P., & Alsdorf, D. E. (2007). Prospects for river
 877 discharge and depth estimation through assimilation of swath-altimetry into a raster-based
 878 hydrodynamics model. *Geophysical Research Letters*, 34(10), 1–5.
 879 <https://doi.org/10.1029/2007GL029721>
- 880 Bates, P. D., Horritt, M. S., & Fewtrell, T. J. (2010). A simple inertial formulation of the shallow
 881 water equations for efficient two-dimensional flood inundation modelling. *Journal of*
 882 *Hydrology*, 387(1–2), 33–45. <https://doi.org/10.1016/j.jhydrol.2010.03.027>
- 883 Biancamaria, S., Durand, M., Andreadis, K. M., Bates, P. D., Boone, A., Mognard, N. M., et al.
 884 (2011). Assimilation of virtual wide swath altimetry to improve Arctic river modeling.
 885 *Remote Sensing of Environment*, 115(2), 373–381. <https://doi.org/10.1016/j.rse.2010.09.008>
- 886 Biancamaria, Sylvain, Lettenmaier, D. P. ., & Pavelsky, T. M. . (2016). The SWOT Mission and
 887 Its Capabilities for Land Hydrology. *Surveys in Geophysics*, 37(2), 307–337.
 888 <https://doi.org/10.1007/s10712-015-9346-y>
- 889 Bonnema, M. G., Sikder, S., Hossain, F., Durand, M., Gleason, C. J., & Bjerklie, D. M. (2016).
 890 Benchmarking wide swath altimetry-based river discharge estimation algorithms for the
 891 Ganges river system. *Water Resources Research*, 52(4), 2439–2461.
 892 <https://doi.org/10.1002/2015WR017296>
- 893 Brêda, J. P. L. F., Paiva, R. C. D., Bravo, J. M., Passaia, O. A., & Moreira, D. M. (2019).
 894 Assimilation of Satellite Altimetry Data for Effective River Bathymetry. *Water Resources*
 895 *Research*, 55(9), 7441–7463. <https://doi.org/10.1029/2018WR024010>
- 896 CNES. (2015). SWOT orbit. [https://doi.org/https://www.aviso.altimetry.fr/en/missions/future-](https://doi.org/https://www.aviso.altimetry.fr/en/missions/future-missions/swot/orbit.html)
 897 [missions/swot/orbit.html](https://doi.org/https://www.aviso.altimetry.fr/en/missions/future-missions/swot/orbit.html)

- 898 Desai, S., Rodriguez, E., Fernandez, D. E., Peral, E., Chen, C. W., Bleser, J.-W. De, & Williams,
899 B. (2018). *Surface Water and Ocean Topography Mission (SWOT) Science Requirements*
900 *Document. Rev B*. California. Retrieved from [https://swot.jpl.nasa.gov/docs/D-](https://swot.jpl.nasa.gov/docs/D-61923_SRD_Rev_B_20181113.pdf)
901 [61923_SRD_Rev_B_20181113.pdf](https://swot.jpl.nasa.gov/docs/D-61923_SRD_Rev_B_20181113.pdf)
- 902 Durand, M., Andreadis, K. M., Alsdorf, D. E., Lettenmaier, D. P., Moller, D., & Wilson, M.
903 (2008). Estimation of bathymetric depth and slope from data assimilation of swath altimetry
904 into a hydrodynamic model. *Geophysical Research Letters*, *35*(20), 1–5.
905 <https://doi.org/10.1029/2008GL034150>
- 906 Durand, M., Rodríguez, E., Alsdorf, D. E., & Trigg, M. (2010). Estimating river depth from
907 remote sensing swath interferometry measurements of river height, slope, and width. *IEEE*
908 *Journal of Selected Topics in Applied Earth Observations and Remote Sensing*, *3*(1), 20–31.
909 <https://doi.org/10.1109/JSTARS.2009.2033453>
- 910 Durand, M., Fu, L. L., Lettenmaier, D. P., Alsdorf, D. E., Rodriguez, E., & Esteban-Fernandez,
911 D. (2010). The surface water and ocean topography mission: Observing terrestrial surface
912 water and oceanic submesoscale eddies. *Proceedings of the IEEE*, *98*(5), 766–779.
913 <https://doi.org/10.1109/JPROC.2010.2043031>
- 914 Durand, M., Gleason, C. J., Garambois, P. A., Bjerklie, D., Smith, L. C., Roux, H., et al. (2016).
915 An intercomparison of remote sensing river discharge estimation algorithms from
916 measurements of river height, width, and slope. *Water Resources Research*, *52*(6), 4527–
917 4549. <https://doi.org/10.1002/2015WR018434>
- 918 Dutra, E., Gianpaolo, B., Jean-Christophe, C., Munier, S., Burke, S., Fink, G., et al. (2017).
919 *Report on the improved water resources reanalysis Deliverable*. Retrieved from
920 [http://earth2observe.eu/files/Public_Deliverables/D5.2 - Report on the Improved Water](http://earth2observe.eu/files/Public_Deliverables/D5.2_Report_on_the_Improved_Water_Resources_Reanalysis_(WRR_tier_2).pdf)
921 [Resources Reanalysis \(WRR tier 2\).pdf](http://earth2observe.eu/files/Public_Deliverables/D5.2_Report_on_the_Improved_Water_Resources_Reanalysis_(WRR_tier_2).pdf)
- 922 Emery, C., Biancamaria, S., Boone, A., Ricci, S., Rochoux, M., Pedinotti, V., & David, C.
923 (2019). Assimilation of wide-swath altimetry observations to correct large-scale river
924 routing model parameters. *Hydrology and Earth System Sciences Discussions*, (June), 1–40.
925 <https://doi.org/https://doi.org/10.5194/hess-2019-242>
- 926 Esteban-Fernandez, D. (2017). *SWOT mission performance and error budget. JPL Publication*
927 (Vol. 2018-April). Retrieved from <https://pdms.jpl.nasa.gov/>
- 928 Evensen, G. (2003). The Ensemble Kalman Filter: Theoretical formulation and practical
929 implementation. *Ocean Dynamics*, *53*(4), 343–367. [https://doi.org/10.1007/s10236-003-](https://doi.org/10.1007/s10236-003-0036-9)
930 [0036-9](https://doi.org/10.1007/s10236-003-0036-9)
- 931 Evensen, G. (2009). The ensemble Kalman filter for combined state and parameter estimation.
932 *IEEE Control Systems*, *29*(3), 83–104. <https://doi.org/10.1109/MCS.2009.932223>
- 933 Fjørtoft, R., Gaudin, J. M., Pourthié, N., Lalaurie, J. C., Mallet, A., Nouvel, J. F., et al. (2014).
934 KaRIn on SWOT: Characteristics of near-nadir Ka-band interferometric SAR imagery.
935 *IEEE Transactions on Geoscience and Remote Sensing*, *52*(4), 2172–2185.
936 <https://doi.org/10.1109/TGRS.2013.2258402>
- 937 Garambois, P. A., & Monnier, J. (2015). Inference of effective river properties from remotely
938 sensed observations of water surface. *Advances in Water Resources*, *79*, 103–120.
939 <https://doi.org/10.1016/j.advwatres.2015.02.007>

- 940 Gleason, C. J., & Smith, L. C. (2014). Toward global mapping of river discharge using satellite
941 images and at-many-stations hydraulic geometry. *Proceedings of the National Academy of*
942 *Sciences*, *111*(13), 4788–4791. <https://doi.org/10.1073/pnas.1317606111>
- 943 Gupta, H. V., Kling, H., Yilmaz, K. K., & Martinez, G. F. (2009). Decomposition of the mean
944 squared error and NSE performance criteria: Implications for improving hydrological
945 modelling. *Journal of Hydrology*, *377*(1–2), 80–91.
946 <https://doi.org/10.1016/j.jhydrol.2009.08.003>
- 947 Hersbach, H., Peubey, C., Simmons, A., Berrisford, P., Poli, P., & Dee, D. (2015). ERA-20CM:
948 A twentieth-century atmospheric model ensemble. *Quarterly Journal of the Royal*
949 *Meteorological Society*, *141*(691), 2350–2375. <https://doi.org/10.1002/qj.2528>
- 950 Hock, R. (1998). *Modelling of glacier melt and discharge*. ETH Zurich.
951 <https://doi.org/https://www.research-collection.ethz.ch/handle/20.500.11850/143428>
- 952 Hock, R., & Holmgren, B. (2005). A distributed surface energy-balance model for complex
953 topography and its application to Storglaciären, Sweden. *Journal of Glaciology*, *51*(172),
954 25–36. <https://doi.org/10.3189/172756505781829566>
- 955 Hunt, B. R., Kostelich, E. J., & Szunyogh, I. (2007). Efficient data assimilation for
956 spatiotemporal chaos: A local ensemble transform Kalman filter. *Physica D: Nonlinear*
957 *Phenomena*, *230*(1–2), 112–126. <https://doi.org/10.1016/j.physd.2006.11.008>
- 958 Kalman, R. E. (1960). A New Approach to Linear Filtering and Prediction Problems. *Journal of*
959 *Basic Engineering*, *82*(1), 35. <https://doi.org/10.1115/1.3662552>
- 960 Kling, H., Fuchs, M., & Paulin, M. (2012). Runoff conditions in the upper Danube basin under
961 an ensemble of climate change scenarios. *Journal of Hydrology*, *424–425*, 264–277.
962 <https://doi.org/10.1016/j.jhydrol.2012.01.011>
- 963 Lee, H., Durand, M., Jung, H. C., Alsdorf, D., Shum, C. K., & Sheng, Y. (2010).
964 Characterization of surface water storage changes in Arctic lakes using simulated SWOT
965 measurements. *International Journal of Remote Sensing*, *31*(September 2017), 14–3931.
966 <https://doi.org/10.1080/01431161.2010.483494>
- 967 Marcus, W. A., & Fonstad, M. A. (2010). Remote sensing of rivers: The emergence of a
968 subdiscipline in the river sciences. *Earth Surface Processes and Landforms*, *35*(15), 1867–
969 1872. <https://doi.org/10.1002/esp.2094>
- 970 Miyoshi, T., Yamane, S., & Enomoto, T. (2007). Localizing the Error Covariance by Physical
971 Distances within a Local Ensemble Transform Kalman Filter (LETKF). *Sola*, *3*(1), 89–92.
972 <https://doi.org/10.2151/sola.2007-023>
- 973 Munier, S., Polebistki, A., Brown, C., Belaud, G., & Lettenmaier, D. P. (2015). SWOT data
974 assimilation for operational reservoirmanagement on the upper Niger River Basin S. *Water*
975 *Resources Research*, *51*(1), 554–575.
976 <https://doi.org/https://doi.org/10.1002/2014WR016157>
- 977 Nash, J. E., & Sutcliffe, J. V. (1970). River Flow Forecasting Through Conceptual Models Part
978 I-a Discussion of Principles*. *Journal of Hydrology*, *10*, 282–290.
979 [https://doi.org/10.1016/0022-1694\(70\)90255-6](https://doi.org/10.1016/0022-1694(70)90255-6)
- 980 O’Loughlin, F. E., Paiva, R. C. D., Durand, M., Alsdorf, D. E., & Bates, P. D. (2016). A multi-
981 sensor approach towards a global vegetation corrected SRTM DEM product. *Remote*

- 982 *Sensing of Environment*, 182, 49–59. <https://doi.org/10.1016/j.rse.2016.04.018>
- 983 Oki, T., & Kanae, S. (2006). Global Hydrological Cycles and World Water Resources. *Science*,
984 5790(313), 1068–1072. <https://doi.org/10.1126/science.1128845>
- 985 Pavelsky, T. M., Durand, M. T., Andreadis, K. M., Beighley, R. E., Paiva, R. C. D., Allen, G. H.,
986 & Miller, Z. F. (2014). Assessing the potential global extent of SWOT river discharge
987 observations. *Journal of Hydrology*, 519(PB), 1516–1525.
988 <https://doi.org/10.1016/j.jhydrol.2014.08.044>
- 989 Pedinotti, V., Boone, A., Ricci, S., Biancamaria, S., & Mognard, N. (2014). Assimilation of
990 satellite data to optimize large-scale hydrological model parameters: a case study for the
991 SWOT mission. *Hydrology and Earth System Sciences*, 18(11), 4485–4507.
992 <https://doi.org/10.5194/hess-18-4485-2014>
- 993 Revel, Ikeshima, Yamazaki, & Kanae. (2019). A Physically Based Empirical Localization
994 Method for Assimilating Synthetic SWOT Observations of a Continental-Scale River: A
995 Case Study in the Congo Basin. *Water*, 11(4), 829. <https://doi.org/10.3390/w11040829>
- 996 Revel, M., Yamazaki, D., & Kanae, S. (2018). Estimating Global River Bathymetry by
997 Assimilating Synthetic SWOT Measurements. *Journal of Japan Society of Civil Engineers*,
998 Ser. B1 (Hydraulic Engineering), 74(4), I_307-I_312.
999 https://doi.org/10.2208/jscejhe.74.I_307
- 1000 Yamazaki, D., Kanae, S., Kim, H., & Oki, T. (2011). A physically based description of
1001 floodplain inundation dynamics in a global river routing model. *Water Resources Research*,
1002 47(4), 1–21. <https://doi.org/10.1029/2010WR009726>
- 1003 Yamazaki, D., Baugh, C. A., Bates, P. D., Kanae, S., Alsdorf, D. E., & Oki, T. (2012).
1004 Adjustment of a spaceborne DEM for use in floodplain hydrodynamic modeling. *Journal of*
1005 *Hydrology*, 436–437, 81–91. <https://doi.org/10.1016/j.jhydrol.2012.02.045>
- 1006 Yamazaki, D., Lee, H., Alsdorf, D. E., Dutra, E., Kim, H., Kanae, S., & Oki, T. (2012). Analysis
1007 of the water level dynamics simulated by a global river model: A case study in the Amazon
1008 River. *Water Resources Research*, 48(9), 1–15. <https://doi.org/10.1029/2012WR011869>
- 1009 Yamazaki, D., De Almeida, G. A. M., & Bates, P. D. (2013). Improving computational
1010 efficiency in global river models by implementing the local inertial flow equation and a
1011 vector-based river network map. *Water Resources Research*, 49(11), 7221–7235.
1012 <https://doi.org/10.1002/wrcr.20552>
- 1013 Yamazaki, D., O’Loughlin, F., Trigg, M. A., Miller, Z. F., Pavelsky, T. M., & Bates, P. D.
1014 (2014). Development of the Global Width Database for Large Rivers. *Water Resources*
1015 *Research*, 50(4), 3467–3480. <https://doi.org/10.1002/2013WR014664>
- 1016 Yamazaki, D., Ikeshima, D., Tawatari, R., Yamaguchi, T., O’Loughlin, F., Neal, J. C., et al.
1017 (2017). A high-accuracy map of global terrain elevations. *Geophysical Research Letters*,
1018 44(11), 5844–5853. <https://doi.org/10.1002/2017GL072874>
- 1019 Yamazaki, D., Ikeshima, D., Sosa, J., Bates, P. D., Allen, G., & Pavelsky, T. (2019). MERIT
1020 Hydro: A high-resolution global hydrography map based on latest topography datasets.
1021 *Water Resources Research*, 2019WR024873. <https://doi.org/10.1029/2019WR024873>
- 1022 Yoon, Y., Durand, M., Merry, C. J., Clark, E. A., Andreadis, K. M., & Alsdorf, D. E. (2012).
1023 Estimating river bathymetry from data assimilation of synthetic SWOT measurements.

- 1024 *Journal of Hydrology*, 464–465, 363–375. <https://doi.org/10.1016/j.jhydrol.2012.07.028>
- 1025 Yoon, Y., Durand, M., Merry, C. J., & Rodriguez, E. (2013). Improving temporal coverage of
1026 the SWOT mission using spatiotemporal kriging. *IEEE Journal of Selected Topics in*
1027 *Applied Earth Observations and Remote Sensing*, 6(3), 1719–1729.
1028 <https://doi.org/10.1109/JSTARS.2013.2257697>
- 1029 Zhao, Q., Ye, B., Ding, Y., Zhang, S., Yi, S., Wang, J., et al. (2013). Coupling a glacier melt
1030 model to the Variable Infiltration Capacity (VIC) model for hydrological modeling in north-
1031 western China. *Environmental Earth Sciences*, 68(1), 87–101.
1032 <https://doi.org/10.1007/s12665-012-1718-8>
- 1033
- 1034 The English in this document has been checked by at least two professional editors, both native speakers of English.
1035 For a certificate, please see:
1036 <http://www.textcheck.com/certificate/248SrS>

A framework for global-scale river discharge estimation by assimilating satellite altimetry

Menaka Revel¹, Daiki Ikeshima², Dai Yamazaki¹, and Shinjiro Kanae²

¹Institute of Industrial Sciences, The University of Tokyo

² Department of Civil and Environmental Engineering, Tokyo Institute of Technology

Contents of this file

Text S1 to S6

Figures S1 to S7

Tables S1

Introduction

In this supporting information, we provide the supplemental text, figures and table for the development of the framework for estimating river discharge by assimilating satellite altimetry. Here we introduce the generating input runoff, data assimilating procedure, empirical localization parameters, estimating SWOT observation error, upstream inflow correction, evaluation of river discharge accuracy using KGE, map of accumulated overpasses per SWOT cycle, variation of NSEAI with accumulated overpasses, and map of assimilation frequency.

Text S1. Generating input runoff forcing

We used HTESSSEL (ECMWF) model runoff out form E2O WRR2 (Dutra et al., 2017) for true simulation. The original runoff was used for simulations in true simulation. The remaining runoff outs were perturbed by multiplying a random number to generate 18 ensembles. Table S1 presets the random values used for each LSM/GHM runoff output for generation ensembles for perfect model experiment and imperfect model experiment.

Table S1: Generation of input runoff forcing for perfect model experiment

Simulation	LSM/GHM	Random Value (Perfect Model experiment)	Random Value (Imperfect Model experiment)
True	HTESSSEL	Original Runoff is used	Original Runoff is used
Corrupted/Assimilated	PCR-GLOBWB	0.93	0.95
		0.97	1.00
		1.04	1.08
	JULES	0.79	0.91
		0.96	0.96
		0.98	1.01
	LISFLOOD	0.88	0.91
		0.94	0.99
		1.08	1.02
	ORCHIDEE	0.81	0.93
		1.03	1.01
		1.12	1.06
	WaterGAP3	0.93	0.85
		0.97	0.97
		1.00	1.18
	W3	0.91	0.85
		0.99	1.01
		1.08	1.05

Text S2: Data assimilation procedure

The LETKF (Hunt et al., 2007; Ott et al., 2004) algorithm was used in this study to efficiently perform data assimilation in global scale. Here, we used the SWOT-observed water surface elevation as the ‘observed variable’ of the data assimilation procedure. The model forecasts were propagated using CaMa-Flood hydrodynamic model. Then the assimilated water state was diagnosed using LETKF algorithm and update the initial conditions for next days` simulation. The water state of the proceeding step (i.e., initial water storage) was computed with data assimilation using LETKF with Equation (A1):

$$x^a = \bar{x}^f + E^f \left[\tilde{P}^a (HE^f)^T (R/w)^{-1} (y^o - H\bar{x}^f) + \sqrt{m-1} (\tilde{P}^a)^{\frac{1}{2}} \right] \quad (S1)$$

where x^a is the assimilated WSE; x^f is the forecasted WSE of each parallel CaMa-Flood ensemble, \bar{x}^f is the mean forecasted value of ensemble members; E^f is the model forecast error covariance matrix, which consist of perturbations which calculated using;

$$E^f = x^f - \bar{x}^f \quad (S2)$$

\tilde{P}^a , and $(\tilde{P}^a)^{\frac{1}{2}}$ were calculated in Equations (S3) and (S4), respectively:

$$\tilde{P}^a = VD^{-1}V^T \quad (S3)$$

$$(\tilde{P}^a)^{\frac{1}{2}} = VD^{-\frac{1}{2}}V^T \quad (S4)$$

where,

$$VDV^T = (m - 1)I/\Delta + (HE^f)^T(R/w)^{-1}HE^f \quad (S5)$$

where m is the number of ensemble members (= 20), I is an identity matrix, Δ is the covariance inflation parameter (estimated adaptively using innovative statistics following Miyoshi, (2011), with background variance of 0.04₂), H is the observation operator which is linearly related to the observation and the state, R is the observation error covariance matrix, which is a diagonal matrix having observation error variances in the diagonal (explained in Appendix C); and w is the observation localization weightage (explained in Appendix B). LETKF applied using the equation (A1) to a ‘empirical local patch’ (explained in Appendix B), which is a small domain around each observation point where the observation has correlations with model state variables. The state variables are independently updated within each empirical local patch.

Text S3: Empirical Localization Parameters

Empirical localization parameters were derived using the spatial auto-correlation of simulated WSEs adaptively. We developed physically-based local patch using CaMa-Flood modelled WSE using runoff simulated by minimal advanced treatments of surface interaction and runoff (MATSIRO: Takata et al., 2003) LSM forced by S14 (Iizumi et al., 2017). The empirical local patches were derived by defining a threshold to the spatial dependency weights calculated by conducting semi-variogram analysis on transformed WSE data. Transformation of WSEs involved three steps: (1) removing trends, (2) removing seasonality, and (3) standardizing. Then, we derived the observation localization weights using Gaussian function using localization lengths corresponds to the threshold defined to the spatial dependency weight to bound the empirical local patch. For further information on deriving physically based adaptive empirical localization parameters, please refer to Revel et al., (2019, 2018b).

Text S4: The SWOT observation error

The SWOT mission sets a goal of 10cm accuracy for water area $\geq 1\text{km}^2$ at the WSE measurement. However, the actual accuracy of future distributing observation data is unclear since it varies with river width, river length, surrounding topography (Durand et al., 2010) or even distance from the satellite track (varies between 4~10cm) (Desai et al., 2018). In this study, we modelled observation error to be normally distributed with zero mean and variance of σ_h .

$$\sigma_h = \begin{cases} \frac{1}{WL} 0.10 & , WL \geq 1.0 \text{ km}^2 \\ \frac{1}{WL} 0.25 & , 1.0 \text{ km}^2 > WL \geq 0.625 \text{ km}^2 \\ 0.25 & , WL < 0.625 \text{ km}^2 \end{cases} \quad (S6)$$

where W and L are river width and river length, respectively. We adopt L to be 1km as we assume only the observations near the outlet of the unit-catchment can be used for data assimilation because CaMa-Flood unit-catchments show internal variability in WSE, especially in steep upstream reaches. We used σ_h as the diagonal components in the observation error covariance matrix in LETKF.

Figure S1 presents the global map of observation error variance calculated using the equation (S6). Most of the upstream reaches where $W < 625 \text{ m}$ are having observation error covariance of 0.25m. Downstream of large rivers such as Amazons, Congo, Ob, Lena, etc. show smaller variances below 0.10m. Therefore, the observation error variance demonstrates a spatial variability.

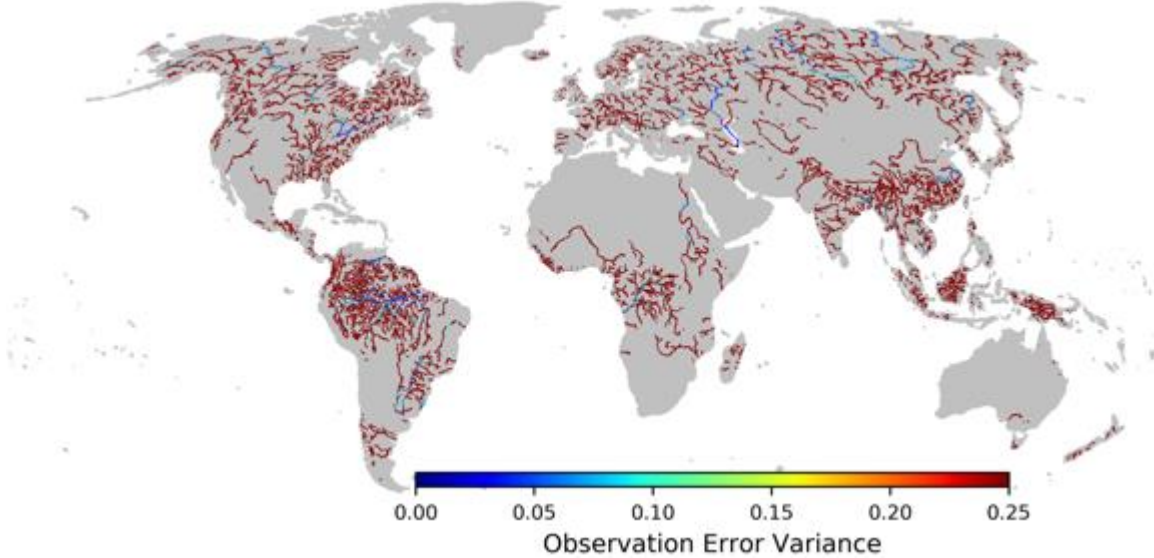


Figure S1. Observation error variance calculated using the equation (S6). Pixels with mean discharge $> 100\text{m}^3/\text{s}$ were used for visualization purposes.

Text S5: Importance of upstream inflow correction

To evaluate the necessity of upstream inflow correction, we performed a ‘partially observed experiment,’ simulating a situation where only part of the observation is available. In this experiment the inflow correction from the upstream was not corrected at all. Here, we used the settings similar to perfect model experiment and set the whole Amazon River basin as an experimental target but disabled the observations westward (upstream) of the midstream location Y (Figure S2b). Therefore, the location Y received local state correction due to its local SWOT observation, but the inflow from upstream was not corrected (Figure S2b). Aside from the observation area, the data assimilation process was identical to that of the perfect model experiment for the whole Amazon River basin. In the partially observed experiment, the improvement by data assimilation at the midstream location Y was mostly lost. In the partially observed experiment, the assimilated discharge was similar to the corrupted discharge at the

location X (Figure S2a). The assimilated discharge was slightly improved at the location Y due to the local assimilations (Figure S2b). The AI was very low, reaching only ~ 0.5 even on days with local observations. On the other hand, the assimilation in the location Z was very successful, because that location is situated sufficiently far away from the unobserved area and the local patch is large enough to receive local observations every day. The spatial distribution of the NSEAI showed that decrease in assimilation efficiency up river reaches around 100km downstream of location Y. But the far downstream reaches were not affected by the unavailability of the observations in upstream. This suggests the propagation of corrected discharges from upstream pixels (i.e., upstream inflow correction) is important. Data assimilation should be applied to the entire upstream region to achieve reasonable estimations of discharge in continental-scale rivers with large drainage areas.

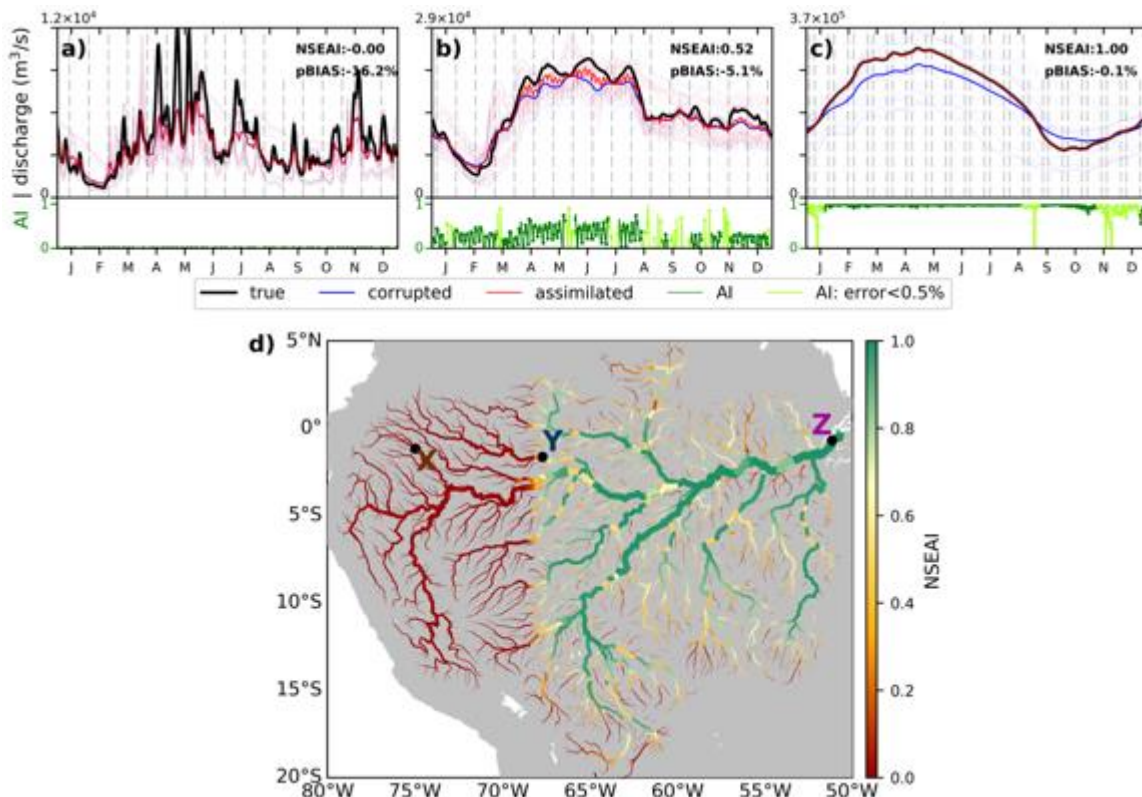


Figure S2. a)-c) Hydrograph for locations X, Y, and Z as in section 4.1.1; and d) NSEAI map for partial observed experiment. Rules are similar to Figure 5.

Text S6. Global River Discharge Estimation Accuracy

a) Perfect model Experiment

To further evaluate the assimilation effectiveness, we compare the KGE metric of assimilated and corrupted simulations at global scale (Figure S3). KGE offers diagnostic insights into the performance of our assimilation framework on estimating river discharge. KGE is a combination of correlation, relative bias, and variability which presets the ability to reproduce of temporal dynamics with preserving flow durations. KGE of assimilated simulation (Figure S3a) results are similar to the global map of NSEAI (Figure 7m), large rivers in low latitudes (i.e. Amazons, Congo, Nile, Mekong, Niger, Mississippi) and rivers in higher latitudes show higher KGE values (>0.8). But the relatively small rivers in south-east Asia, Europe and East Coast of Northern America shows

slightly lower KGE values (0.8~0.6). On the other hand, KGE values of the corrupted simulation has values around 0.4~0.6 due to the difference of the runoff forcing from the true simulation. Almost all the global rivers are having >0.1 difference in KGE between assimilated and corrupted simulation. The KGE difference is also similar to NSEAI (Figure 7m) large low latitude rivers and higher latitude rivers demonstrate large difference (≥ 0.4) and smaller rivers in low latitudes shows lower KGE difference (≈ 0.1). The high KGE difference here means that the data assimilation can benefit the hydrodynamic model, under the assumption that core hydrodynamic model has the correct water physics and river routing system. Therefore, assimilated river discharge shows better simulation efficiency than the non-assimilated simulation (corrupted simulation) in most of the global rivers.

b) Imperfect model Experiment

The KGE-statistic was calculated for evaluating the results of imperfect model experiment and illustrates the insights into the performance of our assimilation framework. Figure S4 shows the global extent of the KGE at imperfect model experiment; KGE of river discharge at assimilated simulation (Figure S4a), corrupted simulation (Figure S4b), and the difference between two simulations (Figure S4c) are presented. Similar to the result of NSEAI (Figure 13), the KGE in the assimilated simulation was large at midstream and downstream locations of the large-scale rivers. Although the upstream locations had a small KGE value, the value rises in the downstream and it becomes almost 1.0 in the downstream. Furthermore, KGE of assimilated simulation are higher than that of corrupted simulation in almost all the global rivers (Figure S4c), difference of KGE was positive at most locations. This denotes that data assimilation of SWOT observation has the potential to correct the simulation even when the model has erroneous geographical parameters (i.e., Manning's Coefficient) and inaccurate runoff forcing. However, an important characteristic of this result must be pointed out: Some locations near river mouth of large rivers had a high KGE value even in the corrupted simulation (Figure S4b). The high KGE values at downstream of the large rivers are due to the coincidence of the true and corrupted discharge well agrees with each other (true and corrupted) (i.e., Congo). In addition, the KGE evaluates the prediction power of model, by focusing on seasonal variation in terms of correlation, relative bias, and variability. As a consequence, KGE was able to remain high at downstream reaches of larges rivers. Those locations tend to have similar seasonal trend (i.e. high-water season happened in the same time) between true and assimilated/corrupted simulation, or have a long period when seasonal trend is almost the same (i.e. discharge at winter season was almost same). Therefore, the high KGE here only means how the data assimilation can benefit the model, under the assumption that core hydrodynamic model error is included in Manning's Coefficient. Hence, the data assimilation is very effective to improve global river discharge under such assumptions. To make data assimilation effective under the real operation of SWOT satellite, hydrodynamic model uncertainties need be decreased.

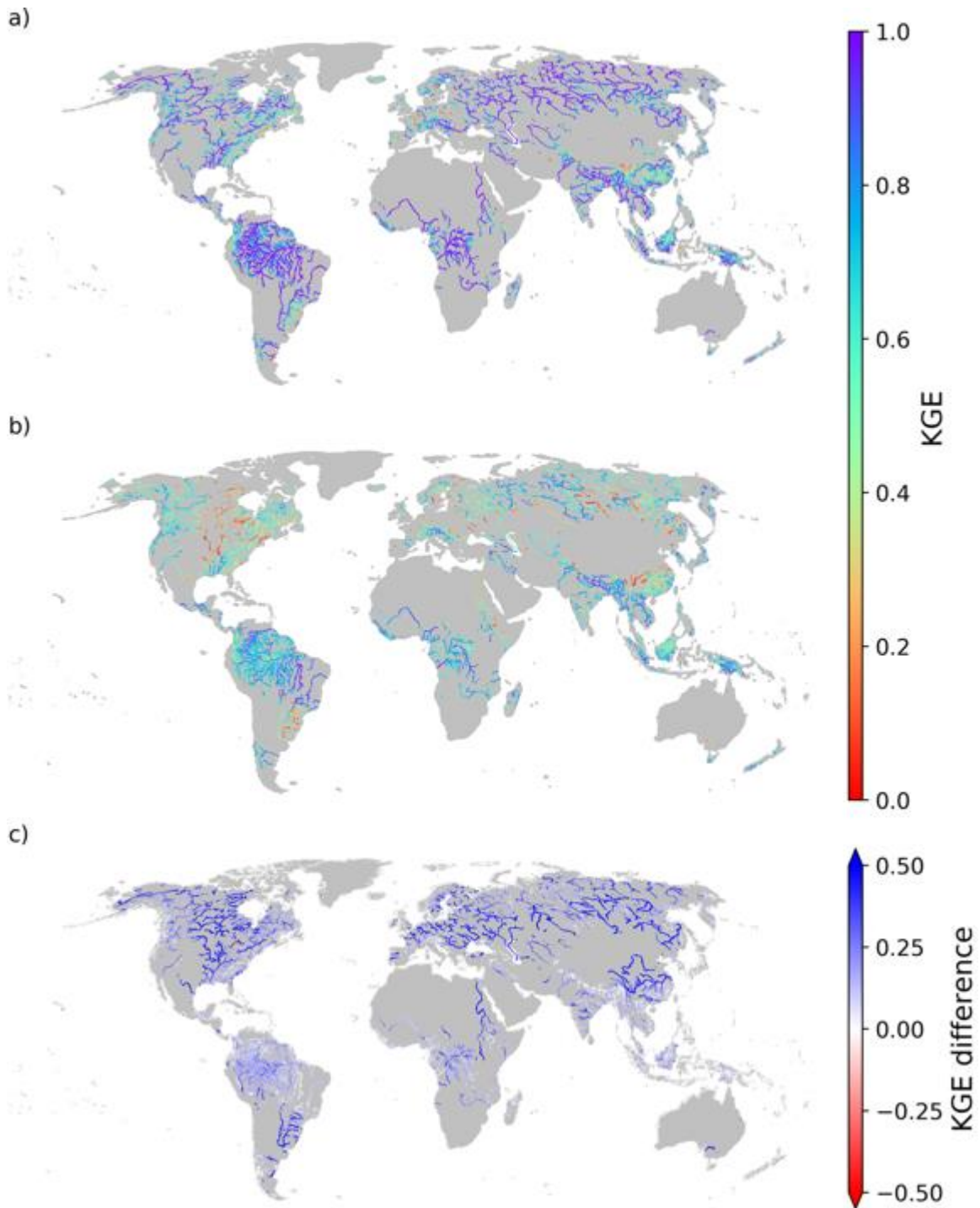


Figure S3. KGE coefficient coefficients of river discharge of a) assimilated and b) corrupted simulations. c) Difference in KGEs for assimilated and corrupted simulations for perfect model experiment. Pixels with mean discharge > 100 m³/s were shown for visualization purposes.

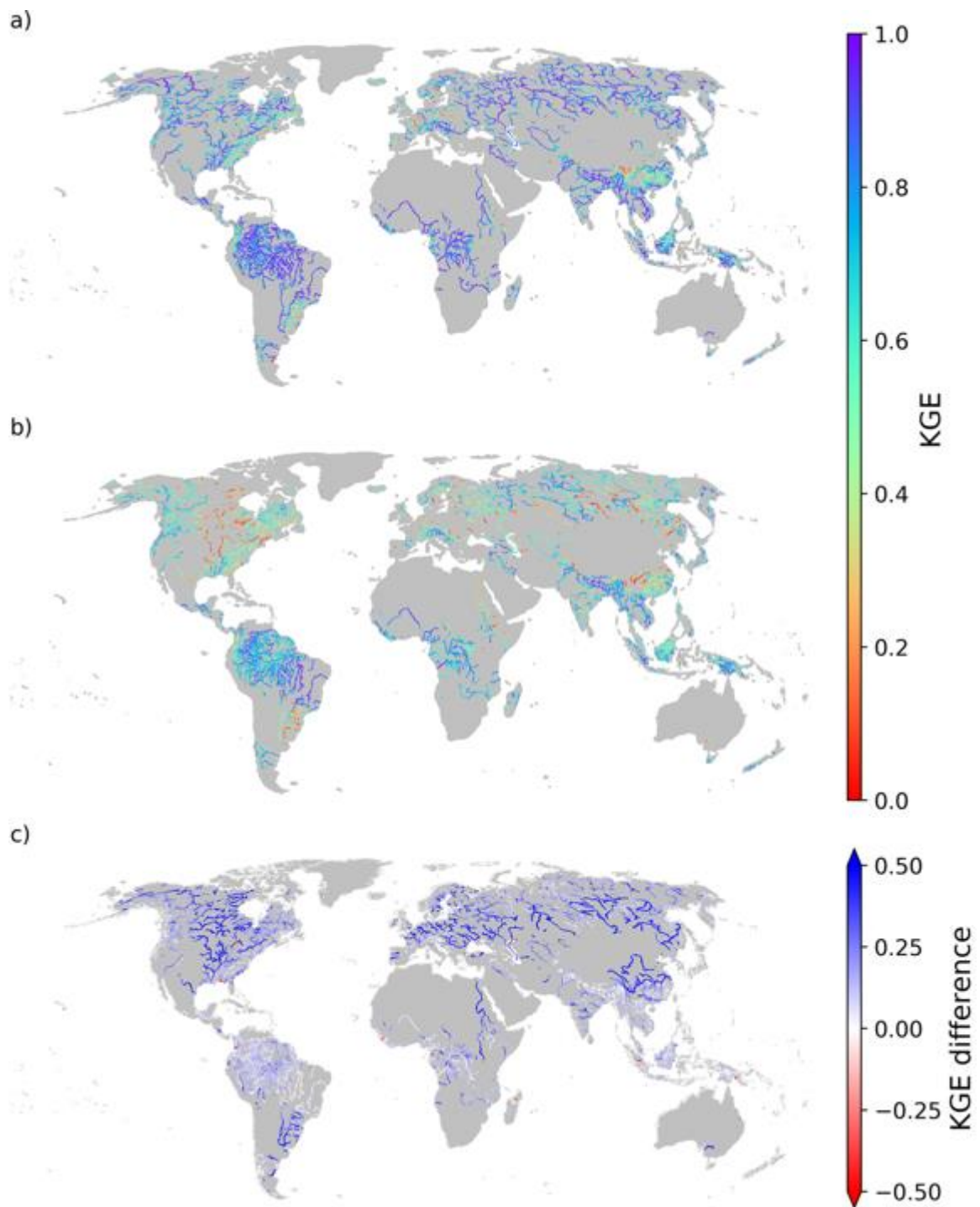


Figure S4. KGE coefficient coefficients of river discharge of a) assimilated and b) corrupted simulations. c) Difference in KGEs for assimilated and corrupted simulations for imperfect model experiment. Pixels with mean discharge > 100 m³/s were shown for visual purposes.

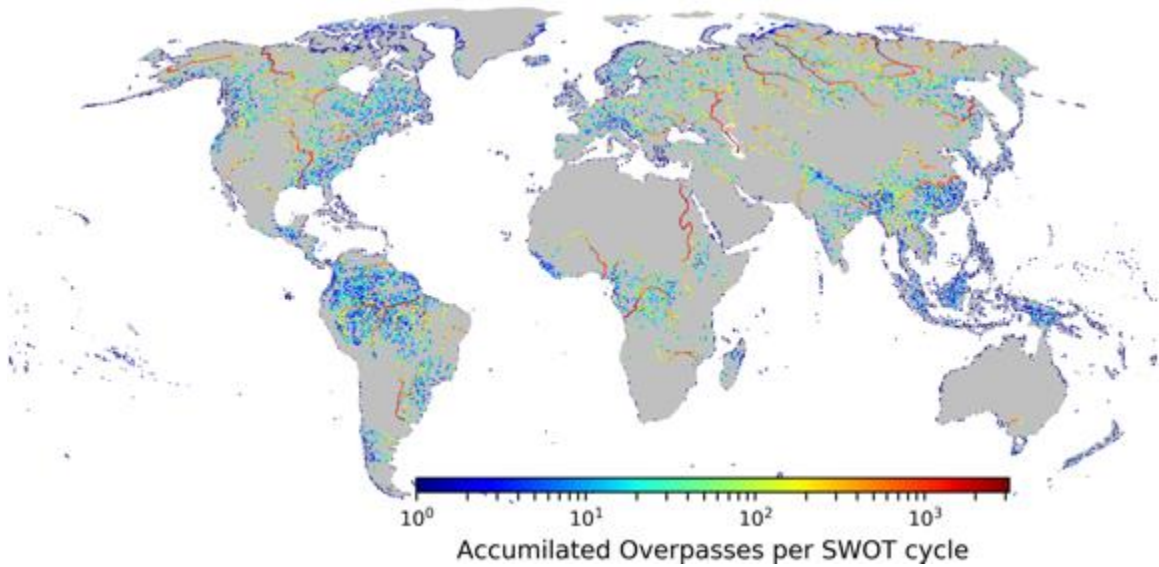


Figure S5: Accumulated Overpasses per SWOT cycle. Pixels with mean discharge > 100 m³/s were shown for visual purposes. Color bar is presented in log scale.

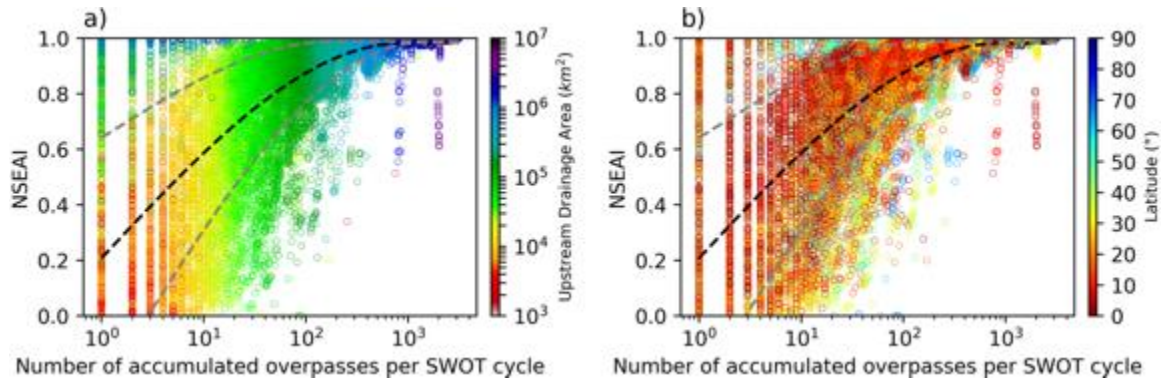


Figure S6: Relationship between accumulated overpasses with NSEAI according to a) upstream drainage area and b) latitude. b) Upstream drainage area with number of accumulated overpasses according to the latitude. The colors represent the upstream drainage area of each pixel in a) and the latitude of each pixel in b) and c).

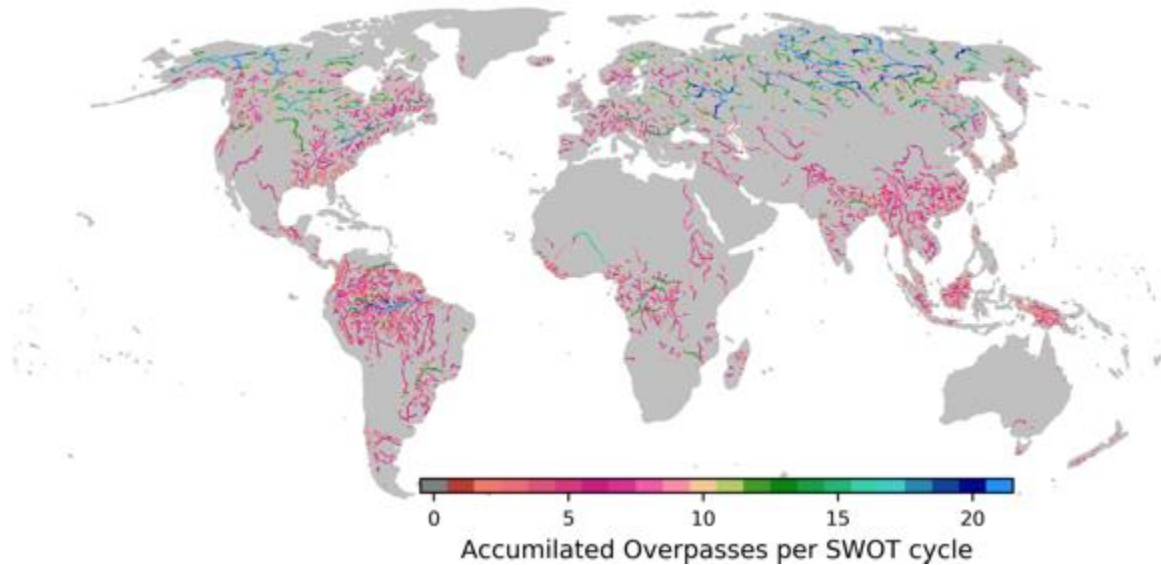


Figure S7: Assimilation Frequency per SWOT cycle. Pixels with mean discharge > 100 m³/s were shown for visual purposes.

Reference

1. Desai, S., Rodriguez, E., Fernandez, D. E., Peral, E., Chen, C. W., Bleser, J.-W. De, & Williams, B. (2018). *Surface Water and Ocean Topography Mission (SWOT) Science Requirements Document. Rev B*. California. Retrieved from https://swot.jpl.nasa.gov/docs/D-61923_SRD_Rev_B_20181113.pdf
2. Durand, M., Fu, L. L., Lettenmaier, D. P., Alsdorf, D. E., Rodriguez, E., & Esteban-Fernandez, D. (2010). The surface water and ocean topography mission: Observing terrestrial surface water and oceanic submesoscale eddies. *Proceedings of the IEEE*, 98(5), 766–779. <https://doi.org/10.1109/JPROC.2010.2043031>
3. Dutra, E., Gianpaolo, B., Jean-Christophe, C., Munier, S., Burke, S., Fink, G., et al. (2017). *Report on the improved water resources reanalysis Deliverable*. Retrieved from [http://earth2observe.eu/files/Public_Deliverables/D5.2 - Report on the Improved Water Resources Reanalysis \(WRR tier 2\).pdf](http://earth2observe.eu/files/Public_Deliverables/D5.2_-_Report_on_the_Improved_Water_Resources_Reanalysis_(WRR_tier_2).pdf)
4. Hunt, B. R., Kostelich, E. J., & Szunyogh, I. (2007). Efficient data assimilation for spatiotemporal chaos: A local ensemble transform Kalman filter. *Physica D: Nonlinear Phenomena*, 230(1–2), 112–126. <https://doi.org/10.1016/j.physd.2006.11.008>
5. Iizumi, T., Takikawa, H., Hirabayashi, Y., Hanasaki, N., & Nishimori, M. (2017). Contributions of different bias-correction methods and reference meteorological forcing data sets to uncertainty in projected temperature and precipitation extremes. *Journal of Geophysical Research*, 122(15), 7800–7819. <https://doi.org/10.1002/2017JD026613>
6. Miyoshi, T. (2011). The Gaussian Approach to Adaptive Covariance Inflation and Its Implementation with the Local Ensemble Transform Kalman Filter. *Monthly Weather*

- Review*, 139(5), 1519–1535. <https://doi.org/10.1109/ICCSCE.2012.6487150>
7. Ott, E., Hunt, B. R., Szunyogh, I., Zimin, A. V., Kostelich, E. J., Corazza, M., et al. (2004). A local ensemble Kalman filter for atmospheric data assimilation. *Tellus A: Dynamic Meteorology and Oceanography*, 56(5), 415–428. <https://doi.org/10.3402/tellusa.v56i5.14462>
 8. Revel, Ikeshima, Yamazaki, & Kanae. (2019). A Physically Based Empirical Localization Method for Assimilating Synthetic SWOT Observations of a Continental-Scale River: A Case Study in the Congo Basin. *Water*, 11(4), 829. <https://doi.org/10.3390/w11040829>
 9. Revel, M., Yamazaki, D., & Kanae, S. (2018). Model Based Observation Localization Weighting Function for Amazon Mainstream. *Journal of Japan Society of Civil Engineers, Ser. B1 (Hydraulic Engineering)*, 74(5), I_157-I_162. https://doi.org/10.2208/jscejhe.74.5_I_157
 10. Takata, K., Emori, S., & Watanabe, T. (2003). Development of the minimal advanced treatments of surface interaction and runoff. *Global and Planetary Change*, 38(1–2), 209–222. [https://doi.org/10.1016/S0921-8181\(03\)00030-4](https://doi.org/10.1016/S0921-8181(03)00030-4)